https://doi.org/10.5194/egusphere-2025-6012
Preprint. Discussion started: 5 December 2025

Modelling the Life–Cycle Impacts of Air Pollution on Tropospheric Ozone and Methane

Calum P. Wilson[1], Michael J. Prather[1]

[1]Department of Earth System Science, University of California, Irvine, Irvine CA, 92697, USA

Correspondence to: Calum P. Wilson (calumw@uci.edu)

Abstract. We calculate the global change in the production of tropospheric ozone (O_3) and loss of methane (CH_4) caused by 45 days of summertime South Korean anthropogenic emissions during the Korea-US Air Quality (KORUS-AQ) mission. Our modelling system consists of three stages: the boundary layer-residual layer (BL-RL) stage processes the emissions, photochemistry, deposition, aerosol reactivity, and transport over terrestrial South Korea at 0.1°x0.1° with hourly resolution. The plume (PL) stage continues to integrate the chemistry of air masses from the BL-RL stage as they are transported offshore, simulating offshore pollution plumes observed by aircraft. After three days of chemical aging in non-diluting plumes, the pollution remnants are dispersed (DP stage) into the background atmosphere and integrated until the pollution disappears. Net O_3 production is diagnosed in each stage using the integrated ozone change and our calculated perturbation lifetimes. In total, these 45 days of South Korean emissions create an excess CH_4 sink of 4.3 Gmol and a net O_3 source of 31.2 Gmol. Scaling these values to annual global emissions suggests around 10% of CH_4 loss and 30% of net O_3 production is attributable to anthropogenic air pollution, but our Korean summertime case may exaggerate the proportions. Reducing plume aging time to 2 days increases these terms by about 10%, and immediate dispersion (no plume aging) more than doubles them. Our model supports the typical result that rapid dispersion of pollution, *e.g.* through coarse resolution, overestimates its impact on tropospheric O_3 and CH_4.

1 Introduction

The degree of future climate change depends on the trajectory of tropospheric ozone (O_3) and methane (CH_4), which are potent greenhouse gases (GHGs). The primary cause of increasing CH_4 abundance over the industrial era is through direct emissions from agriculture and fossil fuel use (see review by Saunois et al., 2025). Secondarily, through the emission of short-lived air pollutants like carbon monoxide (CO), we have altered the dominant atmospheric sink of CH_4, that is, reaction with the hydroxyl radical (OH, e.g., Isaksen and Hov, 1986). Ozone has no primary emissions; its abundance depends mostly on the balance between atmospheric photochemical production and loss. Anthropogenic emissions, especially nitrogen oxides (NO_x = NO + NO_2), volatile organic carbon compounds (VOCs), and CO, drive excess production and increasing abundances of O_3 (Lin *et al*., 1988). Fluctuations in O_3 and its precursor emissions are associated with fluctuations in the global CH_4-OH sink (Zhao *et al*., 2025). In this paper we build a three-stage quasi-3D modelling system that tracks the impact of these pollutants on the net production of O_3 and loss of CH_4 caused by South Korean air pollution. The first *boundary layer-residual layer*

https://doi.org/10.5194/egusphere-2025-6012
Preprint. Discussion started: 5 December 2025

(BL-RL) stage tracks the initial chemistry and transport of pollution in the BL and overlying RL. The second *isolated plume integration* (PL) stage follows air masses that escape from the terrestrial BL-RL domain as pollution plumes in the free troposphere (FT). The third *dispersed pollution* (DP) stage simulates the final chemical decay of pollution after dispersion of the plumes into the background atmosphere, and extracts the O_3 and CH_4 budget terms from this residual pollution.

The test case here uses an intensive set of air pollution data and analysis from the Korea-United States Air Quality (KORUS-AQ) mission, which focused on pollution in South Korea during May-June 2016. KORUS-AQ has generated an extensive body of research on what controls the boundary layer air pollution, particularly O_3, over South Korea (Crawford *et al*., 2021; Eck *et al*., 2020; Lee *et al*., 2022; Miyazaki et al., 2019; Park *et al*., 2021; Peterson et al., 2019; Schroeder et al.; 2020). We use KORUS-AQ data with our new modelling approach to quantify the global impact of this pollution on GHG budgets.

Tropospheric O_3 observations from remote sites, aircraft, ozonesondes, and satellites (Gaudel *et al*., 2018; Ziemke *et al*., 2019) suggest a slight overall increase in global tropospheric O_3 background levels from the 1990s to the 2010s with a pronounced positive trend over East Asia, where O_3 precursor emissions have intensified. Trends in OH-CH_4 loss rate are ambiguous but most global models indicate an increase from 1980 to 2014 of order 10% that is linked to rising NO_x emissions, especially in the lower latitudes (Stevenson *et al*., 2020) caused by rapid industrialisation in East Asia over the last few decades.

We describe the data and tools needed for our modelling system in Sect. 2, then the overall model and its sequence of calculations in Sect. 3. In Sect. 4, we sum the full life-cycle impacts of the Korean emissions on the global GHG budgets and report on the GHG perturbations to tropospheric O_3 and CH_4 caused by 5 weeks of early summer Korean pollution, with the conclusion in Sect. 5.

2 Modelling components and datasets

For the three modelling stages (BL-RL, PL, and DP; see Table 1), we put together (1) emissions data, (2) atmospheric composition observations for both background and polluted regions, (3) the photochemical mechanism and box model, and (4) meteorological data for South Korea over the KORUS period. These are described in the four respective subsections below.

Table 1: Brief description of modelling stages.

Modelling stage	Description
Boundary layer-residual layer (BL-RL)	Emissions, chemistry, horizontal transport, and 3-layer vertical exchange on a 60x60 (0.1°x0.1°) grid domain over South Korea with 1092 terrestrial cells. Air masses transported offshore are collected on 177 PL ghost cells surrounding the coast and combined over 4-hour intervals.
Isolated plume (PL)	Chemical evolution of isolated pollution plumes that depart from the BL-RL terrestrial domain via the PL ghost cells. After three days, all remaining

https://doi.org/10.5194/egusphere-2025-6012
Preprint. Discussion started: 5 December 2025

	pollution and by-products in the plume are dispersed into the free troposphere.
Dispersed pollution (DP)	Chemical evolution of the dispersed, post-plume pollution and their by-products remaining at the end of the PL stage. Both primary emittants and by-product species are integrated at low concentrations to ensure a linear chemistry regime and easy separation of impacts by species in the background troposphere. Pollutants are mixed across four levels (2, 4, 6, and 8 km) every 30 days over a 120-day integration with the impact of any remaining pollution estimated by extrapolation.

2.1 Emission inventories

Three inventories drive emissions of 35 species in our model: KORUS v5 (anthropogenic; Woo *et al*., 2020), GFED5 (biomass burning; Chen *et al*., 2023), and MEGAN v2.10 (biogenic VOCs; Guenther *et al*., 2012). These inventory choices are consistent with the multi-model KORUS-AQ study conducted by Park *et al.* (2021). The KORUS v5 emissions are provided on the same 0.1°x0.1° (latitude by longitude) grid of our boundary layer (BL) model with grid-cell edges at every tenth-degree. The GFED5 (0.25°x0.25°) and MEGAN v2.10 (0.5°x0.5°) grid-cell edges both coincide with KORUS v5 at degrees and half-degrees. Each of our 0.1°x0.1° model grid-cells is mapped onto the emissions grid and collects emissions in proportion to the area of each of the emission cells it spans. All emission cells are fully covered by our BL model cells except at the coastline, where the coarser GFED5 and MEGAN inventories are partially cut off. All KORUS v5 urban and industrial emissions are included however.

2.1.1 KORUS v5 urban and industrial inventories

The KORUS v5 emissions include the explicit species: NO, NO_2, CO (see Fig. 1), ethene, formaldehyde, isoprene, acetaldehyde, methylglyoxal, benzaldehyde, acetone, methyl ethyl ketone (MEK), diacetyl, cresols, phenol, methacrolein (MACR), methyl vinyl ketone (MVK). The inventories also include SAPRC lumped species, which we represent with select surrogate species (see Carter, 2010 for SAPRC-07 documentation). We estimate molar emissions for individual species within SAPRC lumped emission categories using measured abundance ratios from NASA DC-8 airborne BL observations supplemented by emission ratio estimates in the Los Angeles basin (see de Gouw *et al*., 2017). Specifically, RCHO emissions go into propanaldehyde; ALK1, into ethane; ALK2, into propane; ALK3, into *n*-butane; ALK4, into (3/4) *n*-pentane + (1/4) *n*-hexane; ALK5, into *n*-heptane; ARO1, into (2/3) toluene + (1/3) benzene; ARO2, into (2/3) *m*-xylene + (1/3) 1-2-4-trimethylbenzene; OLE1, into propene; OLE2, into butadiene. The KORUS v5 emission inventories used in our BL-RL model are monthly means, but the sources have variability over diurnal- and weekly- cycles, driving a nonlinear response to boundary-layer air chemistry. We therefore apply a unique temporal profile (*i.e.*, a diurnal and week-day activity scale factor; see Crippa *et al*., 2020) for each BL-RL grid cell based on the different sectoral emissions in each cell (see supplementary Fig. S1 and Table S1).

https://doi.org/10.5194/egusphere-2025-6012
Preprint. Discussion started: 5 December 2025

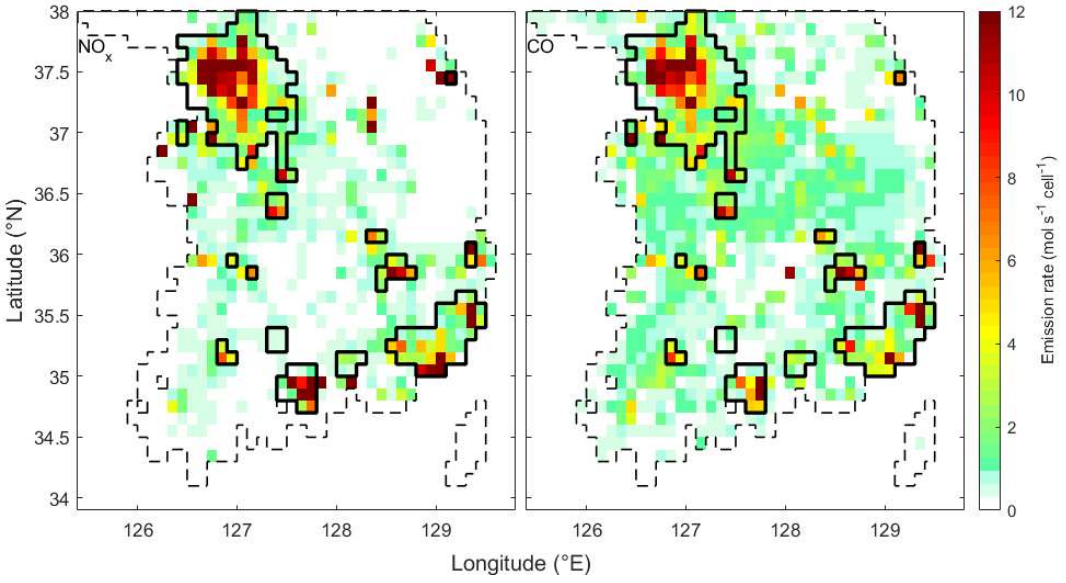

Figure 1: The May 2016 NO_x and CO anthropogenic emission rates from the KORUS v5 inventory (Woo et al., 2020) shown as coloured cells (Same units apply to NO_x and CO). Bold lines enclose "urban" grid-cells in our model-observation comparison that were effectively monitored by five or more NIER ground stations within a ten-kilometre locus during the KORUS-AQ period (see Wilson and Prather, 2025 for ground station distribution). Dashed lines enclose the BL-RL terrestrial domain.

2.1.2 GFED5 biomass burning inventories

We used daily-resolved May and June 2016 biomass burning inventories from GFED5 (0.25°x0.25°, g m^{-2} day^{-1}; see Chen *et al*., 2023), assuming temporally uniform emissions. We include GFED5 emissions of NO, CO, ethane, propane, ethene, propene, isoprene, MEK, benzene, toluene, xylenes (as *m*-xylene), methanol, ethanol, formaldehyde, acetaldehyde, propanaldehyde, methyl glyoxal, formic acid, and glycoaldehyde. Gridded regions lying offshore and outside of the 0.1°x0.1° BL-RL domain are not included.

2.1.3 MEGAN v2.10 biogenic inventories

We use monthly mean MEGAN v2.10 biogenic emission inventories with constant temporal profiles generated for May and June 2010 (0.5°x0.5°, kg m^{-2} s^{-1}; see Guenther *et al*., 2012). We use the following inventories: CO, ethane, propane, ethene, propene, isoprene, toluene, ethanol, formaldehyde, acetaldehyde, acetone, and acetic acid. As in the GFED5 inventories, offshore emissions are assumed to be negligible and excluded from the BL-RL model.

https://doi.org/10.5194/egusphere-2025-6012
Preprint. Discussion started: 5 December 2025

2.2 Atmosphere composition

Observations are used to define the clean-air background chemical composition in our modelling system. The BL-RL stage (Sect. 3.1) uses airborne KORUS-AQ measurements (KORUS-AQ Science Team, 2019) to prescribe a single background composition as a boundary condition for free tropospheric air entrained into the terrestrial BL and RL. Note that our use of a single average KORUS-AQ background composition does not resolve variations in transboundary O_3 and CO pollution entering the Korean peninsula as observed by Miyazaki *et al*. (2019). In the final stage of our modelling sequence (DP stage), we disperse plumes into a vertically-binned remote background environment obtained from the Atmospheric Tomography Mission (ATom) (Sect. 3.3). Our primary model-observation metrics compare the BL concentrations in our 0.1°x0.1° grid cells with a grid-cell averaged values of O_3, CO, and NO_x as observed at the surface NIER sites. See Wilson and Prather (2025) for the methodology of deriving grid-cell averaged data from a set of sites.

2.2.1 KORUS-AQ background air

NASA DC-8 sampled the air above South Korea and the Yellow Sea during 20 days between May 01 and June 11, 2016. Flight paths were coordinated to follow Seoul pollution and other plumes (*e.g.,* from the Daesan industrial complex), and thus distributions of pollutants are positively skewed as a result. All species mole fractions show a clear peak probability at low percentiles, which we use to define "background" air. We calculate the modal concentrations using the Half-Sample Mode of all South Korean flight data and use them to define the BL-RL background composition. These values are not sensitive to the inclusion or exclusion of data sampled within the ERA5-defined boundary layer (Hersbach *et al.,* 2023).

2.2.2 ATom background air

The ATom missions deployed the DC-8 to sample the air over the remote ocean basins and profile the reactivity in the troposphere (Thompson *et al*., 2022). We define the DP background compositions using 10 s merged ATom-4 data (27 April, 29 April, and 21 May 2018) from the modelling data stream (Prather *et al*., 2023) sampled to represent summer Pacific conditions. We take the medians of data partitioned into 2-km-wide altitude bins, centred on 2 km, 4 km, 6 km, and 8 km, using only data flagged as primary and secondary observations; the medians were used to spin-up the DP background air over 365 days (constant summer conditions) in the respective altitude bins (see Table 2 for spun-up concentrations).

Table 2: Background air compositions used in the modelling system.

	KORUS-AQ	ATom steady-state			
Species	**FT**	**2 km**	**4 km**	**6 km**	**8 km**
Column fraction	N/A	35%	27%	21%	17%
Temperature	From ERA5	284	273	260	250

https://doi.org/10.5194/egusphere-2025-6012
Preprint. Discussion started: 5 December 2025

Pressure (hPa)	From ERA5	797	625	484	373
RH (%)	From ERA5	72	46	41	20
CH_4 (ppb)	1930	1910	1890	1880	1870
CO (ppb)	112	115	105	98.5	95.8
O_3 (ppb)	71.5	48.3	56.3	62.6	62.9
NO_x (ppt)	76.3	36.3	31.2	32.1	40.3
PAN (ppt)	249	16.4	48.8	195	236.0
HNO_3 (ppt)	24.9	224	119	79.3	56.6
H_2O_2 (ppt)	233	590	629	417	247
HCHO (ppt)	229	364	218	128	79.6
ethane (ppt)	1550	1320	1200	1070	932
propane (ppt)	155	71.5	57.6	41.8	65.8
n-butane (ppt)	20.0	6.0	4.7	5.0	7.0
Acetone (ppt)	585	448	455	440	498
Acetaldehyde (ppt)	407	15.9	11.5	7.9	6.0
Benzene (ppt)	16.8	22.5	13.5	12.2	15.5
Toluene (ppt)	0.0	0.3	0.2	0.3	0.4

The KORUS-AQ FT (free troposphere) composition provides background air to the BL-RL model and is derived from the Half-Sample Mode of South Korean DC-8 flights. The ATom data are steady-state background compositions used in our DP stage (Sect. 3.3). ATom flight data were sampled on 27 and 29 April, and 21 May 2018 between 30-50°N and 200-235°E, the median 10 s values over 2-km-wide altitude bins centred on 2 km, 4 km, 6 km, and 8 km are used here. Some very low-abundance VOCs (e.g., C_2H_4, isoprene, n-C5-7 alkanes) are initialised in the BL-RL model but not tabulated here.

2.2.2 Surface pollution maps

Surface observations of O_3, CO, and NO_x were recorded by South Korea's National Institute of Environmental Research (NIER) network of 300+ ground stations from 2016/05/02 to 2016/06/11. These measurements have been spatially interpolated via inverse distance weighting (discussed in Wilson and Prather, 2025) and gridded to match our BL-RL model resolution (available at Wilson, 2025).

https://doi.org/10.5194/egusphere-2025-6012
Preprint. Discussion started: 5 December 2025

2.3 Photochemical box model

In all stages of our modelling system we integrate the photochemical evolution of air masses containing South Korean air pollution. For this, we implement the Framework for 0-D Atmospheric Modelling (F0AM v3.1; Wolfe *et al*., 2016) using explicit chemical mechanisms described in Sect. 2.3.1. F0AM is initialised with the mole-fractions of all the chemical species, with constant meteorological parameters (temperature, pressure, and relative humidity), and with *J*-values that we derive from KORUS-AQ observations. Meteorological parameters (pressure and temperature) are used to compute the rate coefficients. During the BL-RL model run, the F0AM chemistry and meteorology is reinitialised hourly in the BL and RL of each grid cell before emissions and transport. During the PL and DP stages, the F0AM model is run over longer periods in a diel cycling mode, updating the *J*-values every half-hour based on the computed solar zenith angle at a standard point near Seoul (37.5°N, 127°E).

2.3.1 Chemical Mechanism

From our set of 35 emitted species, we generate a chemical system of 1610 chemical species and 5000 reactions using the Master Chemical Mechanism (MCM v3.3.1; Bloss *et al*., 2005; Jenkin *et al*., 1997; Jenkin *et al*., 2003; Jenkin *et al*., 2015; Saunders *et al*., 2003). Most of these species are secondary VOCs branching from the decomposition pathways of the primary species.

We found that incomplete reaction mechanisms led to some spurious results in our dispersed pollution modelling. Notably, residual benzene pollution catalysed ozone depletion through secondary products (*2*-hydroxyphenoxy radical, *2*-phenol peroxide, and phenol hydroperoxide) that had an extremely slow termination path. We solved this problem by introducing a first-order loss with a lifetime of 5 days for organic hydroperoxides and hydroxylated species based on the wet deposition timescale for gases with large Henry's Law constants (Bi and Isaacman-VanWertz, 2022). This loss was also included for HNO_3 to avoid unrealistic accumulation in the DP model.

2.3.2 Photolysis frequencies

We use KORUS-AQ observations of J-values under all-sky conditions to model photolysis in our chemical box model (see Hall *et al*., 2018 for instrumental details). We computed the mean J-values centred in 5° solar zenith angle (SZA) bins (15° to 60° bin edges), sampling observations below 1.5 km for the BL-RL model, and above 1.5 km for the PL and DP models. To simulate the diurnal cycle of J-values, F0AM uses the MCM parameterisation: $J = J_{MCM} cos(SZA)^m exp(n/cos(SZA))$, where J_{MCM}, m and n are reaction-specific fitting parameters originally obtained from clear sky radiation modelling (Jenkin et al., 1997; Saunders et al., 2003). Here, we use our SZA-binned KORUS-AQ observations to derive more realistic all-sky *J*-values: $J_{KORUS} = k\, J_{MCM}$, providing F0AM with the correction factors k. We did not attempt to correct the J_{MCM} values that were not observed by DC-8 as these tend to be for less important, low abundance species. See Table 3 for the list of J_{KORUS} and J_{MCM} scale factors, and Fig. 2 for a sample of observed vs. fitted (J_{KORUS}) *J*-values as a function of SZA.

https://doi.org/10.5194/egusphere-2025-6012
Preprint. Discussion started: 5 December 2025

MCM v3.3.1 lacks a photolysis mechanism for peroxyacetyl nitrate (PAN), which is important for PAN loss only in the DP stage in the upper troposphere. We added J-PAN as being proportional to J-$O_3 \rightarrow O(^1D)$ with scale factor 0.014 based on the KORUS J-values and empirical PAN photolysis frequencies (Talukdar *et al*., 1995).

165

Table 3: The photolysis reactions recalibrated in our modelling system.

MCM ID	Reaction	J_{MCM} (s^{-1})	J_{KORUS} <1.5 km (s^{-1})	J_{KORUS} >1.5 km (s^{-1})
J1	J-$O_3 \rightarrow O(^1D)$	6.07E-05	5.66E-05	8.35E-05
J3	J-H_2O_2	1.04E-05	1.01E-05	1.46E-05
J4	J-NO_2	1.17E-02	1.21E-02	1.66E-02
J5	J-$NO_3 \rightarrow O_2$	2.49E-02	2.48E-02	2.86E-02
J6	J-$NO_3 \rightarrow O$	1.75E-01	2.11E-01	2.43E-01
J7	J-HONO	2.64E-03	2.00E-03	2.84E-03
J8	J-HNO_3	9.31E-07	8.66E-07	1.24E-06
J11	J-HCHO→HCO	4.64E-05	4.83E-05	7.57E-05
J12	J-HCHO→CO	6.85E-05	7.06E-05	1.11E-04
J13	J-CH_3CHO	7.34E-06	8.18E-06	1.79E-05
J14	J-C_2H_5CHO	2.88E-05	2.62E-05	5.09E-05
J21	J-CH_3COCH_3	7.99E-07	5.36E-07	8.94E-07
J22	J-MEK	5.80E-06	7.42E-06	1.48E-05
J31	J-CHOCHO→2CO	6.85E-05	1.74E-05	2.72E-05
J32	J-CHOCHO→HCHO	1.03E-05	3.18E-05	4.89E-05
J33	J-CHOCHO→2HCO	3.80E-05	1.11E-04	1.55E-04
J34	J-CH_3COCHO	1.54E-04	1.60E-04	2.43E-04
J35	J-$CH_3COCOCH_3$	3.33E-04	3.63E-04	4.71E-04
J41	J-CH_3OOH	7.65E-06	7.32E-06	1.11E-05
J51	J-CH_3ONO_2	1.59E-06	1.24E-06	1.71E-06
J52	J-$CH_3CH_2ONO_2$	1.91E-06	2.11E-06	2.85E-06

https://doi.org/10.5194/egusphere-2025-6012
Preprint. Discussion started: 5 December 2025

J_{MCM} values are the clear-sky J-value coefficients used in MCM (Saunders et al, 2003). J_{KORUS} are the all-sky coefficients used in our model, fitted using KORUS-AQ J-value observations. MCM also includes photolysis reactions of n- and i-propylnitrate, t-butylnitrate, 2-oxopropyl nitrate, n-butyraldehyde, i-butyraldehyde, (Z)-4-hydroperoxy-2-methyl-2-butenal, MACR, and MVK, which were not reported in KORUS-AQ data.

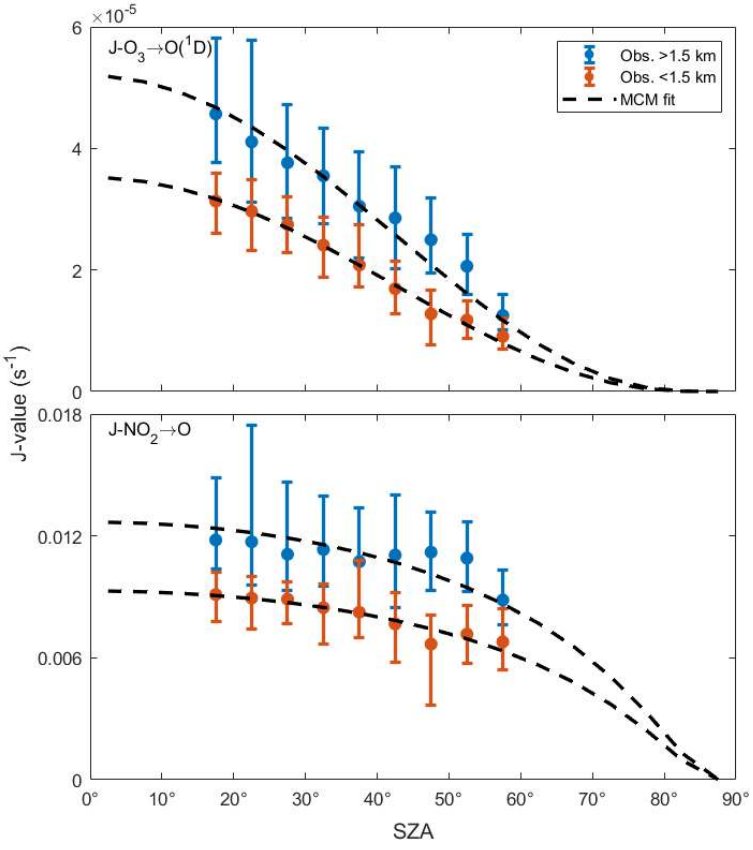

Figure 2: Observed and fitted all-sky J-O3—>O(¹D) and J-NO2 photolysis frequencies. Dots show the mean J-values in 5° SZA bins and whiskers show the root mean square deviations of the upper- and lower- residuals. Dotted lines show the MCM-parameterised J-values scaled to J_{KORUS} values. Data were sampled above (blue) and below (orange) 1.5 km altitude.

2.3.3 Aerosol reactivity

Hydrolysis of N_2O_5, NO_2, and NO_3 on aerosol surfaces is an important sink for NO_x in a polluted environment, effectively converting NO_x to HNO_3, which is irreversible in the BL-RL and PL stages. Aerosol-HO_2 reactions also reduce HO_x (OH + HO_2) and subsequently ROOH radicals. The first-order rate coefficient for aerosol reactivity with molecule X is given by $(1/4)\rho_A v_X \gamma_X$ (Yan *et al*., 2019), where ρ_A is aerosol surface area density, v_X is the mean thermal velocity of X, and γ_X is the surface reaction probability. We use Lamarque *et al*. (2012) aerosol reactivities ($\gamma_{N2O5} = 0.1$; $\gamma_{NO} = 0.0001$; $\gamma_{NO3} = 0.001$;

https://doi.org/10.5194/egusphere-2025-6012
Preprint. Discussion started: 5 December 2025

$\gamma_{HO2} = 0.2$), which are taken to be independent of aerosol composition. Aerosol surface area densities were inferred from KORUS-AQ Laser Aerosol Spectroscopy (LAS) in situ 10 s measurements of size-resolved particle number density (Nault *et al.*, 2018). We average the surface area densities over the entire KORUS-AQ period for altitude ranges of 0.0-1.5 km (BL-RL stage), 2±1 km (PL and DP stages), 4±1 km, 6±1 km, and 8±1 km (DP stage). Thermal velocities for the four species were computed using the mean ERA5 meteorology for the BL-RL stage and ATom mean temperature profiles for PL and DP stages (see Table 2). Final aerosol reactivity values used in the different modelling stages are shown in Fig. 3.

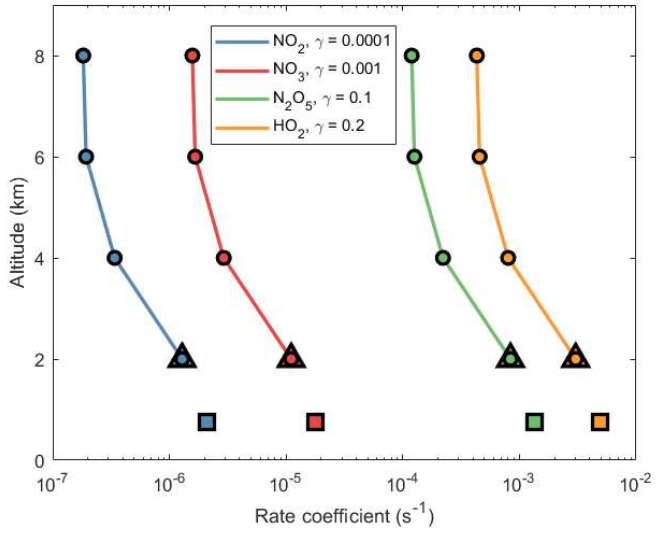

Figure 3: Aerosol reactivity rate coefficients used in our model stages. These first-order loss coefficients for NO2, NO3, N2O5, and HO2 are computed from mean aerosol surface area concentrations and temperatures profiled by DC-8 during the KORUS-AQ mission and used for the BL-RL (squares; 0.0-1.5 km altitude), PL (triangles; 2±1 km), and DP (circles; 2±1, 4±1, 6±1, and 8±1 km) stages (see Table 2). Aerosol surface areas are from KORUS-AQ LAS data (Nault et al., 2018).

2.3.4 Surface deposition

Surface deposition is a sink of O_3 and NO_2 in our hourly BL chemical integrations. The BL-RL model uses a simple dry deposition velocity (v_d, cm s^{-1}) for O_3 and NO_2 in each grid cell based on a fixed land surface classification over the KORUS period. The deposition first-order loss rate (s^{-1}) in the BL is calculated hourly as v_d divided by BL height (cm). To map the land cover over the BL-RL grid domain, we use 32 land cover classifiers as defined by the Land Cover Classification System (LCCS, 2017). From the LCCS 1/360°x1/360° pixels, we calculate the fractional coverage of each classifier in our 0.1°x0.1° model cells. We group the 32 classifiers into 8 super-classifications used by Jia *et al.* (2016) (see Table 4 for our super-classifications and their constituent LCCS classifiers). We combine our classification fractional areas to calculate average v_d values for O_3 and NO_2 as shown in Fig. 4.

https://doi.org/10.5194/egusphere-2025-6012
Preprint. Discussion started: 5 December 2025

Table 4: Average dry deposition velocities (v_d) for land surface categories.

Super-classifications	LCCS classifiers	NO_2 v_d (cm s^{-1})	O_3 v_d (cm s^{-1})
Cropland	*cropland (5)*	0.07	0.43
Grassland	*grassland*	0.11	0.27
Evergreen	*evergreen (4)*	0.28	0.47
Mixed forest	*tree_mixed*	0.13	0.51
Deciduous	*deciduous (6)*	0.13	0.4
Tree-shrub	*shrubland (3)* *mosaic (3)*	0.2	0.34
Urban	*urban* *lichens_and_moss* *bare_areas (3)* *sparse (4)*	0.03	0.03
Water	*water (3)* *flooded* *ice*	0.01	0.03

Values shown are based on data from field campaigns covering different terrain classifications (Zhang et al., 2009; Adon et al., 2013; Zhang et al., 2002; Simpson et al., 2001; Brook et al., 1999). Data represent diel averages over the campaign periods. For super classifications with the LCCS classifiers, see text.

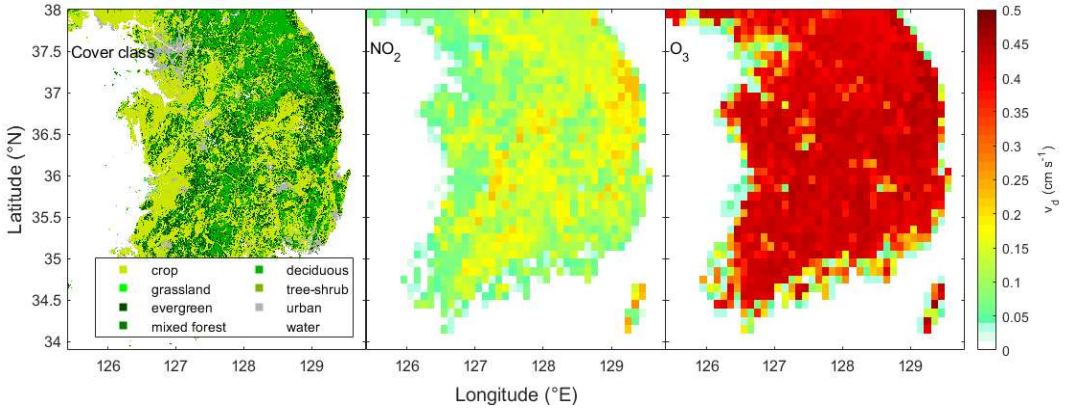

https://doi.org/10.5194/egusphere-2025-6012
Preprint. Discussion started: 5 December 2025

Figure 4: Land cover classes and dry deposition maps. (a) Land cover classes show our super classifications based on the LCCS classifiers plotted at the native 1/360°x1/360° resolution. Dry deposition (v_d) rates for O_3 (b) and NO_2 (c) at model resolution (0.1°x0.1°) are derived from the area-weighted super-classifications and average deposition velocities in Table 4.

2.4 ERA5 meteorology

Our BL-RL stage uses hourly, 0.25°x0.25° ERA5 Reanalysis 2D fields for boundary layer height and surface pressure (Hersbach *et al.,* 2023) plus 3D fields for temperature, specific humidity, u, and v wind (Hersbach *et al*., 2017). The ERA5 data are point-values defined at grid centres (*e.g*. 37.50°N, 127.00°E at Seoul) and at hybrid (η) vertical level centers. ERA5 pressure is indexed on vertical level edges. Our BL and RL columns are discretized and vertically aligned with these edge-level coordinates at the start and end of every hourly timestep in the model, and the 3D fields are averaged separately in the BL and RL columns to produce 2D mean column values for winds, temperature, and humidity. We only use the lower atmospheric ERA5 data, from k = 99 (~4.5 km altitude) to k = 137 (surface; see Table 5).

The BL always consists of at least one ERA5 layer above the surface, and the RL – if it exists – consists of at least one layer atop the BL column. The BL and RL columns each have a single chemical mixture with a mean pressure and temperature averaged over their constituent ERA5 layers. To obtain these fields at model resolution (0.1°x0.1°), we interpolate the grid-centred ERA5 data to our model grid-cell centres via bicubic convolution and assume these data points represent the area mean. The ERA5 nocturnal BL height falls to a mean minimum height of 175 m over the Korean peninsula, and locally as low as 24 m, leading to unrealistically concentrated emissions. We mitigate this problem by prescribing a minimum BL height of 200 m in our model.

Table 5: The ERA5 vertical coordinates used in the BL-RL model stage.

ERA5 level index (l)	Lower edge-level quantities				Mid-level quantities		
	η_A (Pa)	η_B	p (hPa)	z (m)	δp (hPa)	T (K)	δz (m)
99	16262	0.411	574	4566	NA	NA	NA
100	15597	0.438	594	4287	20.6	268.9	278
101	14898	0.466	615	4017	20.6	270.4	270
102	14173	0.494	636	3755	20.5	271.8	262
103	13428	0.522	656	3503	20.4	273.2	253
104	12668	0.549	676	3260	20.1	274.5	243
105	11901	0.577	696	3028	19.7	275.7	232
106	11133	0.604	715	2806	19.3	276.9	222

https://doi.org/10.5194/egusphere-2025-6012
Preprint. Discussion started: 5 December 2025

107	10370	0.630	734	2595	18.8	278.0	211
108	9618	0.656	752	2394	18.2	279.0	200
109	8880	0.681	769	2205	17.5	280.0	189
110	8163	0.705	786	2026	16.9	280.9	179
111	7470	0.728	802	1858	16.1	281.8	168
112	6804	0.750	818	1701	15.4	282.7	158
113	6169	0.771	832	1553	14.6	283.5	148
114	5564	0.791	846	1415	13.9	284.3	138
115	4994	0.810	859	1286	13.1	285.1	129
116	4457	0.827	872	1167	12.4	285.8	120
117	3956	0.844	883	1055	11.6	286.4	111
118	3489	0.859	894	952	10.9	287.1	103
119	3057	0.874	905	856	10.2	287.6	96
120	2659	0.887	914	768	9.5	288.2	88
121	2294	0.900	923	686	8.8	288.7	82
122	1962	0.911	931	611	8.2	289.1	75
123	1659	0.922	939	541	7.6	289.5	69
124	1388	0.932	946	478	7.1	289.9	64
125	1143	0.941	952	419	6.5	290.2	59
126	926.5	0.949	958	365	6.0	290.5	54
127	735.0	0.957	964	315	5.6	290.7	50
128	568.1	0.963	969	270	5.1	290.9	45
129	424.4	0.970	974	228	4.7	291.1	42
130	302.5	0.975	978	190	4.3	291.2	38
131	202.5	0.980	982	155	4.0	291.4	35
132	122.1	0.985	986	123	3.7	291.6	32

https://doi.org/10.5194/egusphere-2025-6012
Preprint. Discussion started: 5 December 2025

133	62.8	0.989	989	94	3.4	291.7	29
134	22.8	0.992	992	67	3.1	291.9	27
135	3.76	0.995	995	43	2.8	292.0	24
136	0.000	0.998	998	20	2.6	292.0	22
137	0.000	1.000	1000	0	2.4	292.0	20

ERA5 levels index mid-level meteorological variables (e.g. T and q) and lower-edge pressure levels (p) defined by hybrid parameters η_A and η_B, for a surface pressure of 1000 hPa. Layer thicknesses (δz) are computed from the hydrostatic equation using pressure thicknesses (dp), T, and q (not shown), then integrated from the surface to obtain the lower-edge heights (z).

2.4.1 Vertical discretisation (BL and RL)

Our BL-RL model uses mass-weighted (δp) column averages for temperature, specific humidity, and horizontal wind fields. To average these variables for the BL and RL, we align the BL and RL edges in our model to nearest ERA5 vertical edge levels in each gridded interpolated ERA5 atmospheric column over the terrestrial domain. Each model time step starts and finishes with a discretised BL+RL column, where the BL consists of an integral number of ERA5 levels based on mass, and the RL, if it exists at the time, consists of an integral number of ERA5 levels atop the BL. When the ERA5 BL height (m) changes with time, we adjust the top of the BL to the closest ERA5 edge level (in metres). If the BL column expands to envelop higher levels, it collects all the pollution in the entrained RL levels; if it envelops levels above the RL, it collects FT air. If the BL contracts, it leaves behind discrete layers of residual pollution that are mixed with the RL column. This step represents the effective vertical transport in the model.

When the ERA5 surface pressure field changes each hour, the ERA5 edge-level pressures shift, resulting in misaligned initial and final pressure levels. This effect is hardly noticed because the horizontal transport of BL and RL levels separately results in BL and RL mass that do not align with the new edge levels. Every hourly timestep, after horizontal and vertical transport, we realign the BL-RL and RL-FT (or BL-FT) interfaces with the standard ERA5 levels (*rediscretisation*) and remap the air mass from the intermediate BL+RL+FT columns to the new partition (*remapping*). The BL and RL masses adjust during horizontal transport. If the new BL mass (determined by the new BL height and ERA5 level edges) exceeds the transported BL+RL burdens, then the RL is fully entrained and some FT air is remapped to the BL. If the transported BL+RL mass exceeds the new BL mass, then some air is remapped into the RL. If any RL mass remains after vertical transport, the RL-FT interface is rediscretised by adding the ERA5 levels upward from the new BL-RL interface to the first level that fully encapsulates the RL mass. Some background FT air is remapped to the RL during this process. While we keep track of the BL and RL air mass during horizontal transport and vertical remapping, the critical elements being transported are the moles of primary and secondary pollutants. When we add FT air to the BL or RL, we likewise keep track of the pollutants from this relatively clean air. During this process, no pollutants are mixed into the FT: the accumulated pollutants, including those

https://doi.org/10.5194/egusphere-2025-6012
Preprint. Discussion started: 5 December 2025

emitted into the BL and entrained from the FT, can only leave the South Korean peninsula horizontally as polluted plumes to be tracked in the PL stage.

We calculate the temperature and specific humidity of the BL and RL in each grid-cell as mass-weighted averages. Horizontal wind velocities in the BL and RL are also -mass-weighted at ERA5 grid centres, but we compute column-averaged winds over the same set of levels over the entire peninsula to avoid spatial discontinuities. For each timestep, BL winds are vertically averaged from the surface to the median top-of-BL level, and RL winds, from the median top-of-BL level to the median top-of-RL level.

3 Models

Previous chemistry-transport model studies of East Asian air pollution, such as Wild *et al*. (2004), found that "*ozone formation in the boundary layer and free troposphere outside the region of precursor emissions dominates total gross production from these sources in springtime, and that it makes a big contribution to the long range transport of ozone, which is greatest in this season.*" These studies, and subsequent global modelling studies of O_3 production from air pollution, have relied on the concept of odd-oxygen for calculating O_3 production and loss terms, but this approach gives false lifetimes and incorrectly diagnoses production rates and their sensitivities, as was recently demonstrated by Prather and Zhu (2024). These global models would have correctly calculated the perturbation to O_3 but would have incorrectly diagnosed the production and loss budgets. Here, we design a model that explicitly calculates perturbation lifetimes of O_3 and can thus diagnose the net production of O_3, and loss of CH_4, that is driven by pollutants. We can separately calculate the O_3 budgets from pollution plumes as seen by aircraft (Cho *et al*., 2021; Miyazaki *et al*., 2019; Crawford *et al*., 2019; Guo *et al*., 2023; Bourgeois *et al*., 2020 and 2021; Jacob *et al*., 2003; Hsu *et al*., 2004), a noted problem in Wild et al. (2004).

Our hybrid model is quasi-three-dimensional, accounting for the geographic variations in BL pollution over South Korea. The modelling system follows the chemical evolution of boundary layer pollution as it travels across South Korea (BL-RL stage), continues to chemically age the air masses leaving the peninsula as isolated pollution plumes (PL stage) and finally as dispersed pollution remnants (DP stage) under realistic, but idealized, atmospheric conditions typical of the region. The BL-RL model stage is the most complex, using hourly emissions and meteorology to model the chemical evolution of pollution in the planetary boundary layer as it moves across the South Korean peninsula (see Table 6). We do not explicitly consider the convective transport of BL pollution directly into the FT. Large convective systems lift and disperse BL pollution, however, we follow the horizontal pollution transport evolution across the peninsula and offshore into the PL stage.

The PL stage chemically ages the pollution when BL or RL air masses are first swept offshore. This pollution is collected over 4-hour intervals in BL-RL ghost cells surrounding South Korea, then released as isolated pollution plumes to evolve undiluted for 3 days at 2 km altitude. When these plumes disperse, the remaining primary and secondary pollutants (including O_3) are passed to the dispersed pollutant (DP) stage. Here, we assume that pollutants are dilute enough so that the chemistry of pollutants is first-order and can be calculated separately for each species based on the observed background

https://doi.org/10.5194/egusphere-2025-6012
Preprint. Discussion started: 5 December 2025

composition of the mid-latitude Pacific troposphere. Each pollutant's impact is independent of the other pollutants. The DP stage mixes the remaining pollutants from the PL stage uniformly across the 1-9 km altitude range and calculates the O_3 and CH_4 budget terms across four altitude ranges (2±1, 4±1, 6±1, and 8±1 km) to. Every 30 days the pollutants are remixed vertically. After 120 days the chemically active pollutants are mostly gone and a simple extrapolation from the last 30 days can be used to estimate any remaining O_3 and CH_4 reactivity. The sequence of modelling operations is summarised in Table 6, and details of the calculations are described below.

Table 6: A summary of the modelling operations acting on South Korean air pollution.

Processes	Timestep	Description
Boundary layer-residual layer (BL-RL) stage (3.1)		
Chemical integration (3.1.1)	1 hr	Update the solar time (*J*-values) and integrate the chemistry (including dry deposition and aerosol loss) in BL and RL columns. Update the BL and RL chemical concentrations, keep track of the moles of primary and secondary pollutants, and diagnose the reactivity of O_3 and CH_4.
Emissions (3.1.2)	1 hr	Deposit an hour of emissions into the BL of each grid cell.
Horizontal transport (3.1.3)	10 min	Follow the horizontal transport of BL and RL masses in six 10-min substeps with remapping onto the standard grid cells at each substep. For the ghost cells, accumulate transported air mass for 4 hours before releasing as a pollution plume (PL).
Vertical remapping (3.1.4)	1 hr	For standard cells, remap the BL and RL mass onto new standard ERA5 levels, partitioning the BL based on the new BL height.
Isolated pollution plume (PL) stage (3.2)		
Initialisation	4 hr	Collect pollution leaving the peninsula in BL-RL offshore ghost-cells during horizontal transport. Release the accumulated air and pollutant mass accumulated over 4 hour intervals from each ghost cell as an individual pollution plume.
Daily integration	1 day	Integrate 24-hour diel chemistry of each plume. Update solar zenith angle at 30 minute resolution. Keep track of the daily O_3 and CH_4 reactivities as well as the evolution of primary and secondary pollutant mass. End integration after 3 days.
Dispersed pollution (DP) stage (3.3)		
Disperse remnants	30 days	Follow the final destruction of the primary and secondary pollutants released

https://doi.org/10.5194/egusphere-2025-6012
Preprint. Discussion started: 5 December 2025

		from the PL stage. Mix a unit, linear perturbation of each major remnant species over 4 layers in the background atmosphere and integrate the O_3 and CH_4 reactivities in the same manner as the PL stage, but in four altitude bins.
	30 days	Mix the remaining pollutants into the 4 standard layers every 30 days and continue the 30-day integration until 120 days have elapsed.
	120 days	Tabulate the final, linearised O_3 and CH_4 perturbations for the remnant species, summed over the four atmosphere layers and 30-day periods. Extrapolate the O_3 and CH_4 perturbations from any remaining secondary CO based on the tabulated CO results. Combine the linearised O_3 and CH_4 perturbations with the 3-day plume remnants.

The discrete processes for the three modelling stages are outlined and briefly described. The timesteps indicate the frequency at which operations are performed.

3.1 Boundary layer-residual layer (BL-RL) stage

The BL-RL stage is set on a latitude-longitude grid of 60x60, 0.1°x0.1° geographical cells centred on South Korea. The BL-RL domain comprises 1092 terrestrial grid-cells where emissions and chemistry are processed, and 177 ghost-cells on the model domain circumference that collect air transported out of the BL-RL domain. When diagnosed, the BL and RL always consist of a discrete number of contiguous ERA5 layers. The BL always contains the layers from 0-200 m above surface, while RL may be completely absent if fully entrained by the BL, or fully ventilated by horizontal transport. The chemical concentrations in the BL and RL are calculated from the tracked number of moles of pollutants, and the molar dry air column burdens, which are proportional to the sum of the δp levels (see Table 5) and grid-cell quadrangle areas.

Within the model domain, the BL and RL columns in each cell have a unique mix of pollutants, with a single pressure, temperature and chemical composition. The BL collects, transports, and chemically evolves fresh emissions while depositing O_3 and NO_2 to the surface. The RL collects, transports, and chemically evolves air detrained from the BL when the BL height drops. All air outside the terrestrial cells and in layers above the BL+RL has FT background composition, and this air can enter the BL columns when the BL height rises above the RL layer, or when offshore air is horizontally transported into the terrestrial grid cells. A careful budget is kept of chemical species entering the model domain via the FT.

3.1.1 Photochemistry

The first BL-RL model step is the F0AM integration of hourly chemistry for each BL and RL column. F0AM integrates the chemistry in each column using the pollutant mixing ratios, MCM v3.3.1 rate coefficients, first-order deposition rates (dry, aerosol, and scavenging), mean column meteorology (temperature, pressure, relative humidity), SZAs computed from grid-cell coordinates and model UTC time, and KORUS-AQ all-sky *J*-values (see Sects. 2.3-2.4). Temperature and pressure are used to calculate the reaction rates and convert mixing ratios to number densities. Budget data such as chemical tendencies and individual chemical rates are integrated at the sub-hourly F0AM ODE solver resolution and diagnosed every hour.

https://doi.org/10.5194/egusphere-2025-6012
Preprint. Discussion started: 5 December 2025

3.1.2 Emissions

Each hourly timestep, after the chemical integration, we inject an hour of emissions into each grid cell given the species-wise emission rates (mol s^{-1}) of the KORUS v5, GFED5, and MEGAN v2.10 inventories (see Sects. 2.1.1-2.1.3). For the KORUS v5 inventories, we multiply the mean emission rate (resolved monthly) by a diurnal activity scale factor (resolved hourly) and a day-of-week activity scale factor (weekday, Saturday, or Sunday). These scale factors are unique to each grid cell and derived from the individual emission sector activities in the cell (see Sect. 2.1.1).

For cells with intense emission sources, the operator splitting poses a challenge. If we release an hour of emissions into each grid-cell before the chemistry operator, then the hour-long chemistry calculation begins with a mass of unrealistically concentrated, undispersed air pollution rather than a ventilated stream of emissions processed continuously. With our current operator sequence, the emissions are transported partly to neighbouring cells before the chemical generation of secondary pollutants. The obvious remedy is to cut the overall operator time-steps to *e.g.* 30 min or even 10 min. Unfortunately, restarting the chemistry integration every 10 minutes is computationally prohibitive for us. However, we can test the errors caused by our operator sequencing by cutting the overall time step to 1/2 hr and 1/4 hr for a 3-day test case. From 1 hr to 1/4 hr timestepping, we found a +1.3% and +0.9% error in total CH_4 and O_3 reactivity; and from 1/2 hr to 1/4 hr, the errors decrease but change sign, indicating convergence.

3.1.3 BL and RL horizontal transport.

Horizontal advection moves the BL and RL across the peninsular grid, brings in FT background air from offshore, and sends pollution plumes from the model domain to the offshore PL ghost cells. Each hour, we calculate two sets of grid-resolved 2D (u, v) wind fields, one for the BL and one for the RL. We transport each on separate planes following the BL and RL (u, v) trajectories to their new locations. These trajectories are fixed over the 1-hour step and are generally not straight lines. We move each BL or RL cell in a sequence of six 10-minute sub-steps, where each sub-step splits the original (source) cell into four new (receptor) grid cells as depicted in Fig. 5. The four parts of the BL/RL cells are reassembled onto the standard grid cell, and the process is repeated for the remaining 5 sub-steps. Cell fractions transported offshore are collected as pollution plumes for the PL stage. The choice of 10-minute advection timesteps enables intense emissions to horizontally ventilate quasi-continuously along curved trajectories over the hour.

To compute the trajectory paths for each terrestrial BL cell, we adopt a fixed effective BL height for the one-hour time step for all South Korea based on the median top-of-BL height for terrestrial cells (see Sect. 2.4.1). Using this set of fixed ERA5 levels, we calculate a pressure-weighted set of (u, v) fields at the centroids of the 60x60 model cells with bicubic interpolation. The u and v components are converted to angular velocities in per-second degree arcs that remain fixed over the 1-hour time step. We then transport the BL cell to new centroid positions along the arcs via 10-minute Euler-forward-stepping linear trajectories. These 10-minute trajectories are linear and non-deformational and thus allow for easy partitioning into four cells at their destination as shown in Fig. 5. The series of 10-minute sub-stepping trajectories allows realistic curved and

https://doi.org/10.5194/egusphere-2025-6012
Preprint. Discussion started: 5 December 2025

350 deformational motion of the BL cells (i.e., convergence or divergence). Then we partition the source BL air mass (and pollutants therein) into four receptor cell BLs in proportion to the source-receptor area overlaps. This is repeated 6 times over the hour. The RL cells are transported likewise, but using the RL-weighted (u, v) fields, where the pressure-weighting of the winds ranges from the median South Korean top-of-BL level-edge to the median top-of–RL level edge.

The interpolated BL and RL (u, v) winds will almost certainly include convergence or divergence and thus receptor 355 cells will collect more or less than 100% of their area fractions. This discrepancy, along with the discrepancies in source- and receptor- BL column masses, leads to a change in BL+RL dry-air column masses after each 10-minute step. BL and RL air mass and source cell pollution that is transported outside the terrestrial domain is accumulated in the ghost-cell closest to the transported centroid coordinates. We track BL and RL outflows to ghost cells separately, but do not vertically remap or discretise them in the ghost cell. Their chemical evolution in the PL stage is treated separately and identically. Inshore flow to 360 terrestrial cells provides FT air to the BL in proportion to the source-receptor area-overlap and receptor BL column mass. We assume RL pollution does not mix with FT air, so we ignore offshore transport into the terrestrial RL.

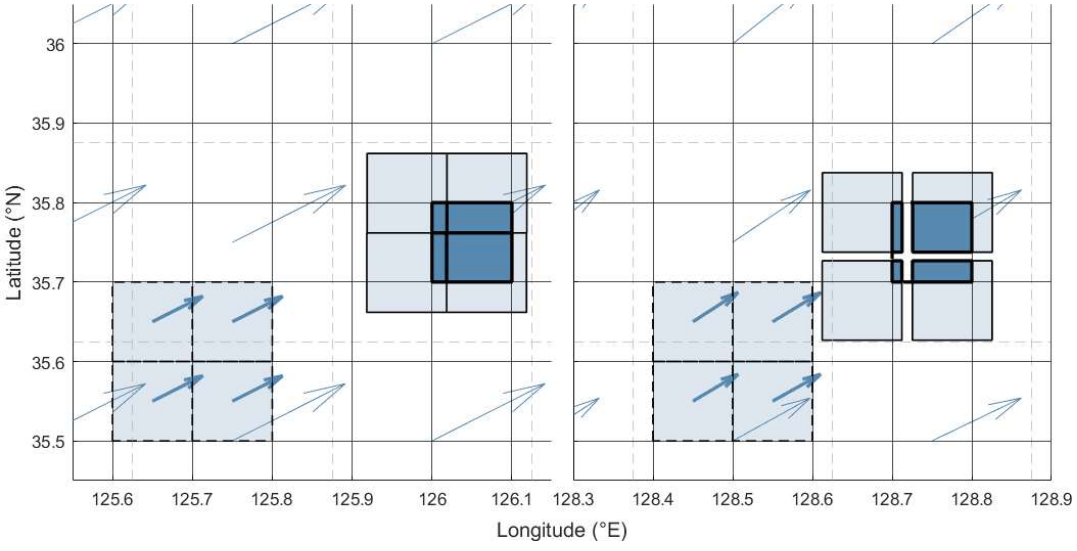

Figure 5: A schematic of the BL-RL model horizontal transport. Left: the receptor BL column (dark-blue square) receives air mass from 365 four source BL columns (dashed light-blue squares) transported north-eastward in a straight-line path without divergence over a 10-minute step. The new receptor BL comprises a fraction of each source BL column in proportion to the rectangular overlap after transport (dark-blue rectangular areas). Right: As described above, but in a divergent wind field. The four adjacent light-blue cells separate, and the white cross-shaped area in the receptor cell is vacuous. Wind vectors (arrows) are sampled centrally in the ERA5 grid (dashed grid), vertically averaged in the BL, and interpolated to the model grid cell centroids (bold arrows) to determine the source cell trajectories.

https://doi.org/10.5194/egusphere-2025-6012
Preprint. Discussion started: 5 December 2025

3.1.4 Vertical remapping of the BL-RL

With each 1-hour timestep, we have new ERA5 fields for surface pressure and BL height. As described in Sect. 2.4, the new BL height in meters is used to select the new upper BL edge-level in hPa that most closely matches it. If the BL top after horizontal transport lies above the new one (i.e., a falling BL) then the polluted air mass between the new and old BL is added to and mixed with the overlying RL, creating a new RL if none initially existed. If the new BL top lies above the new one (i.e., a rising BL) then the new BL takes in the mass from the RL. If the available RL mass is insufficient then the BL entrains mass and chemical pollutants (including O_3) from the FT. The BL-RL-FT exchange during the vertical remapping step depends on BL height dynamics (*i.e.*, the change in BL height over the last hour), but is also convoluted by horizontal transport (*i.e.*, convergence or divergence in BL and RL trajectories). The BL and RL columns transported into a grid-cell at the end of the time step will not align with the BL in the receptor grid-cell and model levels and must be remapped as illustrated in Fig. 6. In Fig. 6.a, the new BL air mass (right columns) exceeds the BL+RL masses (left columns), and thus it entrains all pollutants in the BL and RL plus those in the FT needed to make up the total air mass (thick black bars). In Fig. 6.b, the new BL mass sits in the middle of the transported RL, and thus some of the transported RL goes into the new BL, and the remainder, into the new RL. The new RL is rounded up to the next level by adding FT mass (and FT pollutants) into the RL. In Fig. 6.c, the new BL mass is less than the transported BL mass, and the excess is placed into a new RL.

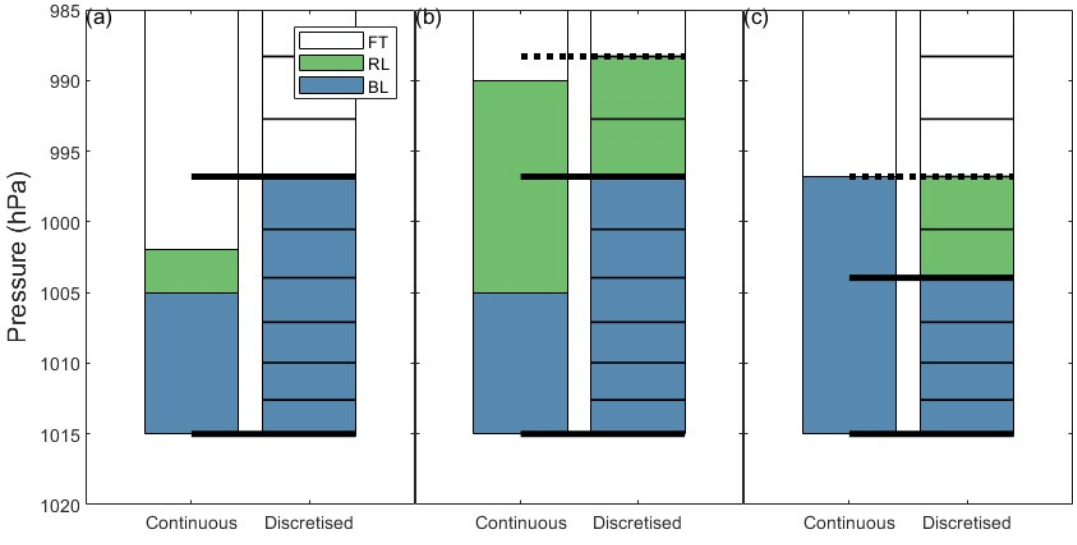

Figure 6: Schematic of the BL-RL model vertical remapping. The four panels show the re-gridding of a BL (blue) and RL (green) air masses (left) that have been left in a new cell (right) after the horizontal transport step. The new cell is marked with the pressure edge levels based on the new surface pressure and a BL mass (blue) based on the new BL height, see text. Three examples here are: (a) incoming BL+RL mass is less than new BL mass, so BL+RL+FT is pulled into the new BL and the RL disappears; (b) BL+RL mass exceeds new BL mass, so some RL is absorbed into the new BL and a new, smaller RL is created with some FT air incorporated; and (c) incoming BL mass exceeds the new BL and so an RL is created.

https://doi.org/10.5194/egusphere-2025-6012
Preprint. Discussion started: 5 December 2025

3.1.5 Surface observations

We compare our BL results for O_3, CO, and NO_x with grid-cell averaged observations derived from the NIER network (Sect. 2.2.2) using the methodology of Wilson and Prather (2025). In supplement S2 we show model-observation statistics and plots, sampled in "urban" grid-cells that were effectively observed by five or more NIER sites. The time series is decomposed into four meteorological phases described by Peterson *et al.* (2019), named as *dynamic* (01-16 May), *anticyclone* (17-22 May), *transport* (25-31 May), and r*ex-block* (01-07 June). Our model performance and diurnal cycles for O_3, CO, and NO_x were consistent with a separate study that used the WRF-Chem v4.4 chemistry-transport model (CTM) driven by the same KORUS v5 inventory (see supplemental Table S2 and Figs. S2-6; see Fig. 2 from Kim *et al*., 2024). Modelled O_3 correlated well with observations (R = 0.6-0.8), NO_x, less so (R = 0.5), and CO was uncorrelated (R = 0.3). The mean biases of model daytime O_3 ranged from -1 ppb (anticyclone and transport phases) to +21 ppb (dynamic and rex-block phases); model NO_x bias ranged from -7 ppb to -17 ppb, and model CO had extreme biases of -120 to -240 ppb. Ozone overestimates occurred during meteorological phases with high transboundary influence (Miyazaki *et al.*, 2019), and this factor was not reflected in our model boundary conditions. Nitrogen oxide measurements from the NIER network are known to have an "NO_2 artifact" that introduces a +4 ppb bias in our data (Jung *et al*., 2017), accounting for some of the bias in our model. Our model CO bias is similar to that reported by Kim *et al*. (2024). Compared with DC-8 profiling in the BL, NIER CO data was notably biased by around +100 ppb (Wilson and Prather, 2025), and we believe this identifies a bias problem with the NIER CO data.

3.2 Pollution plume (PL) stage

We assume that pollution leaving South Korea in the RL or BL masses is maintained as an undiluted pollution plume for several days, as often seen in aircraft observations (Crawford *et al*., 2004; Heald *et al*., 2004; Liang *et al*., 2007). Following Prather and Jaffe (1990), we assume that sharp concentration gradients along plume edges are maintained by windshear, largely conserving plume mass and concentrations until its final dissolution. Our model allows for the plume to last for up to three days before it is ultimately sheared and shredded, losing its integrity and dispersing the remaining pollution, highly diluted, into the background atmosphere.

We separately collect the BL and RL air and pollution masses that are transported beyond the terrestrial grid into the 177 ghost cells that line the coast. We collect and release the BL and RL masses from each ghost cell every six hours starting at midnight local time. Considering the 45-day KORUS period and the 2 spindown days to clear pollution at the end, there are a maximum of 47 x 6 x 177 = 49,914 plumes in the BL and RL each, but because not all ghost cells collect pollution every 4 hours, the numbers are 32,954 and 30,632 respectively. Each plume is integrated at a fixed temperature, pressure, and relative humidity (284 K, 797 hPa, and 72%) based on the ATom climatology at 2 km altitude (Table 2). The same F0AM chemical model used in the BL-RL stage is used to integrate a sequence of three 24-hour periods for each plume, starting at the hour of

https://doi.org/10.5194/egusphere-2025-6012
Preprint. Discussion started: 5 December 2025

its release. *J*-values were rescaled using KORUS-AQ all-sky scale factors above the clouds (see Sect. 2.3.2) and updated every half-hour. The pollution content and accumulated reactivities of O_3 and CH_4 were stored daily for each plume.

A key uncertainty in the PL stage arises from the largely unknown dynamical timescales of plume dilution; these timescales are important because the total O_3 and CH_4 reactivities increase with dilution. Our base case asserts a 3-day dynamical lifetime for all plumes, but with our daily diagnostics for each plume we can re-evaluate our cumulative GHG budgets assuming 2 days, 1 day, or 0 days of plume aging. We find that aging pollution beyond 3 days only marginally affects the budget terms, and we discuss the impact of shorter aging times in Sect. 4. Fig. 7 shows the evolution of plume nitrogen and VOC species that contribute significantly to DP stage reactivity.

To provide a reference value for the reactivities in the BL-RL and PL stages, we repeat the PL integrations for control plumes initialized from a control BL-RL run with no anthropogenic emissions (KORUSv5 and GFED5). Subtracting the control run budgets from the standard run budgets yields the budget perturbations induced by South Korean emissions.

https://doi.org/10.5194/egusphere-2025-6012
Preprint. Discussion started: 5 December 2025

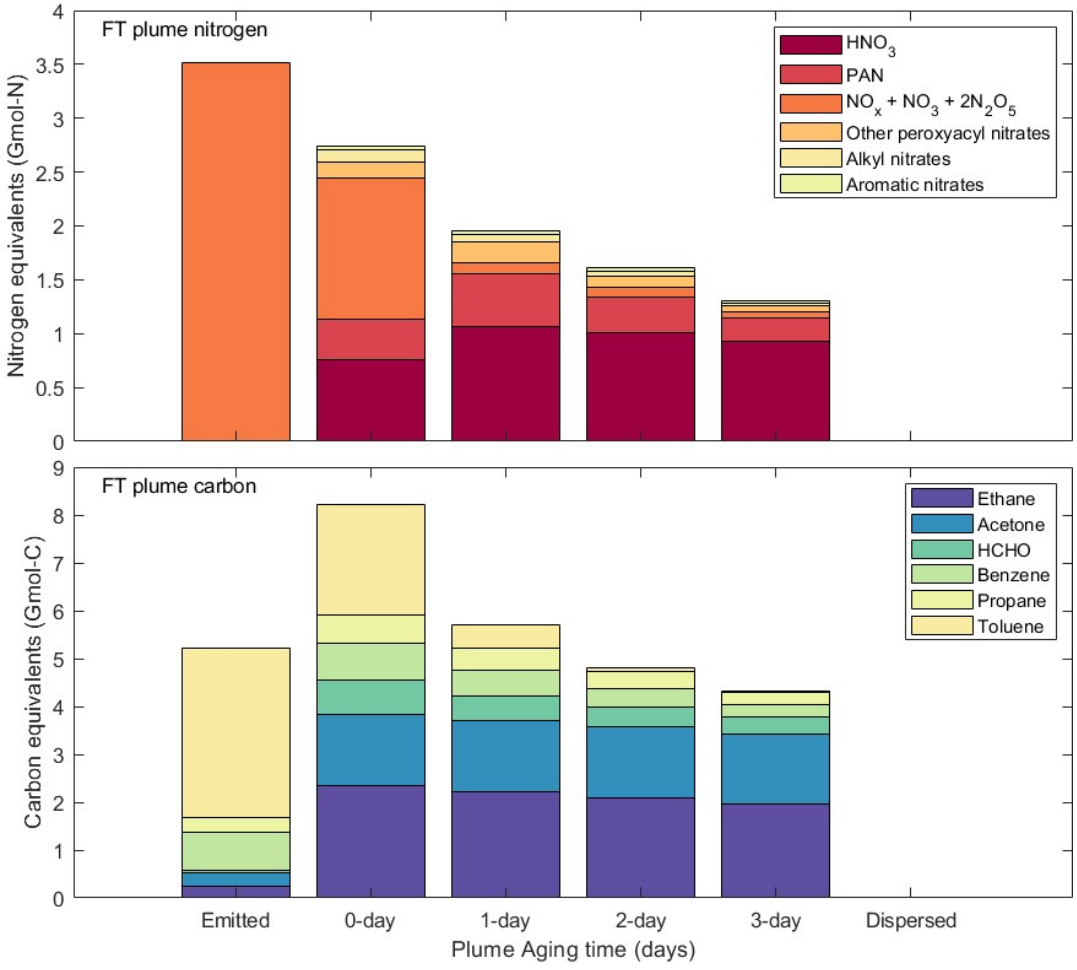

Figure 7: Total NOy-nitrogen (Gmol-N, top) and VOC-carbon (Gmol-C, bottom) pollution content emitted in the BL-RL stage and aged in the PL stage. "Emitted" designates initial anthropogenic emissions, and "0-day" aging shows the pollution exiting the BL-RL stage, which includes biogenic emissions and background air. Only species with high impact on the O_3 and CH_4 budgets in the DP stage are shown. Loss of total nitrogen occurs through nitrate aerosol formation and gas-phase HNO_3 scavenging. Loss of total carbon occurs through formation of non-plotted secondary VOCs, carbon monoxide, and carbon dioxide. Most ethane in the plume is from background air (i.e., not emitted) which does not impact the budgets.

3.2.1 Airborne observations

The DC-8 aircraft sampled South Korean pollution on 20 days in May and June 2016, vertically profiling the Seoul Metropolitan Area on most flight days and chasing offshore pollution plumes based on tracer-transport forecasting. We expect the composition of freshly exported plumes from the BL-RL model to resemble *in situ* observations in the South Korean BL.

https://doi.org/10.5194/egusphere-2025-6012
Preprint. Discussion started: 5 December 2025

In our comparison, we sum observed reactive N species into NO_y-nitrogen in moles of N, specifically NO, NO_2, PAN, and PPN. We do not include other nitrates such as NO_3 and N_2O_5 as they were not individually observed, but measured in combination with HNO_3 and particulate nitrate. Likewise, we sum all VOCs measured at high frequency (1 Hz) into VOC-carbon in moles of C. VOC-carbon includes ethane, benzene, toluene, isoprene, methacrolein, acetaldehyde, acetone, methyl ethyl ketone, methyl vinyl ketone, and formaldehyde, but not CH_4, CO, or CO_2 (KORUS-AQ Science Team, 2019).

Fig. 8 shows the 2D histograms of NO_y-nitrogen and VOC-carbon in our model plumes aged 0 and 1 day, and in the observations sampled above and below the BL height, as resolved hourly at 0.25° x 0.25° in the ERA5 data. See supplemental Fig. S7 for a map of DC-8 sampling. The dominant plume compositions in the 0-day-aged plumes and BL observations centre on 1.0-3.0 ppb NO_y-nitrogen and 15-25 ppb VOC-carbon, with around +5 ppb more VOC-carbon in the observations. Such a pattern was also observed in transects through Seoul pollution transported west over the Yellow Sea on 22 May. Observations with >10 ppb NO_y-nitrogen were frequent in the densely sampled Seoul Metropolitan Area and also in fresh urban and industrial plumes off the west (22 May and 05 June) and southeast coast (07, 11, 20, and 30 May); modelled plumes with this range of compositions were also found. After 1-day aging, the modelled plumes had a range of NO_y-nitrogen concentrations resembling FT observations, but with greatly diminished abundances of short-lived aldehydes and alkenes. From this comparison, pollution plumes sampled in the FT, primarily offshore from South Korea, were probably aged less than a day.

https://doi.org/10.5194/egusphere-2025-6012
Preprint. Discussion started: 5 December 2025

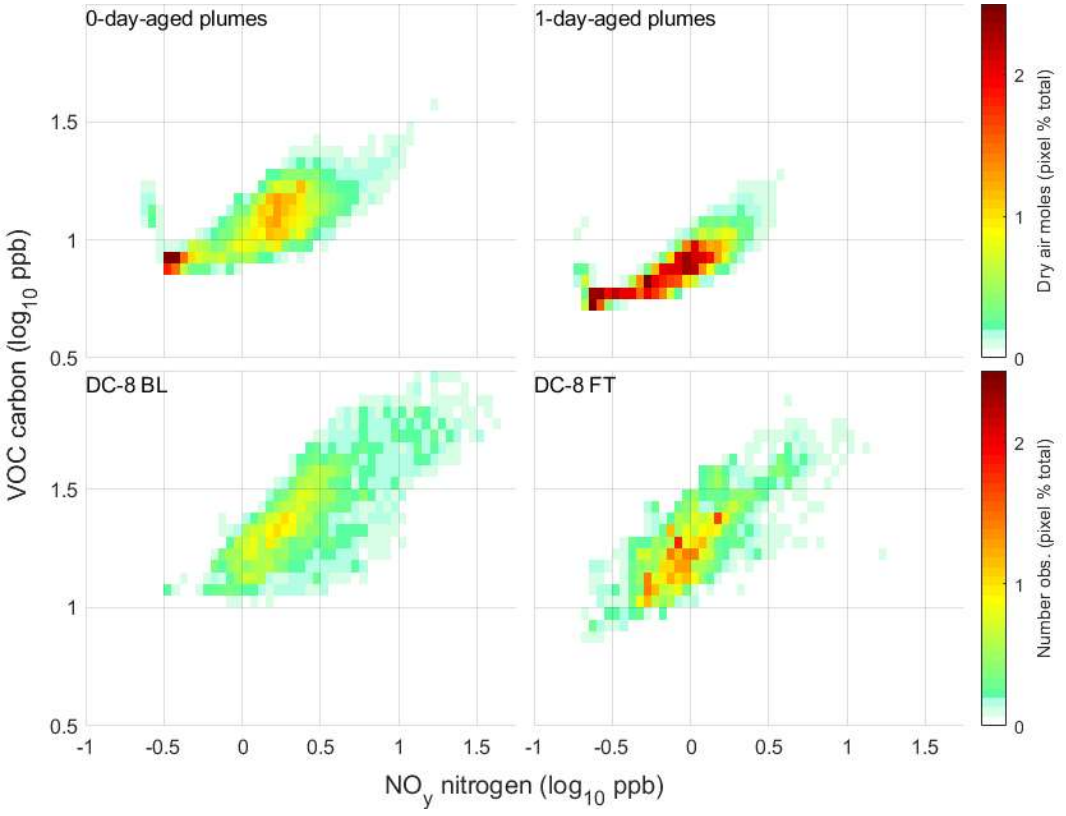

Figure 8: 2D distribution of VOC-carbon vs. NO_y-nitrogen in modelled plumes and DC-8 observations. Shown are modelled plumes aged 0-days (top-left) and 1-day (top-right), and DC-8 observations of the BL (bottom right) and FT (top right). Probability densities (colour bar) are normalised total moles (top) and number of observations (bottom) resolved as pixels of 0.05 $\log_{10}$ ppb width. Geographic sampling of DC-8 data is shown in supplemental Fig. S7.

3.3 Dispersed pollution (DP) stage

We model the DP stage as a linearly separable chemistry problem. Specifically, we assume that the dispersion of a pollution plume results in a perturbation to the atmospheric chemistry that is sufficiently dilute so that the interaction of two pollutants (*i.e.*, the second-order terms) is negligible. The impact of any pollutant is thus in the linear regime and can be scaled from the integration of a small perturbation. We create a look-up table relating moles of O_3 and CH_4 produced or lost per moles of pollutant X dispersed.

The chemical response of the atmosphere to an added pollutant depends on chemical composition, pressure, temperature, *J*-values, aerosols, *etc*. Since we do not model transport in the PL stage, we do not know where the plumes disperse, nor where the remnants are transported afterwards. We choose to disperse the pollutants across four tropospheric layers whose composition is derived from ATom-4 measurements (27 April, 29 April, and 21 May 2018) sampled between

https://doi.org/10.5194/egusphere-2025-6012
Preprint. Discussion started: 5 December 2025

2±1, 4±1, 6±1, and 8±1 km altitude over the northern midlatitude Pacific (see Table 2). At each of the four altitudes we integrate the reactivity of the atmosphere with the addition of 0.1 ppb of pollutant and then subtract a control run made without the added pollutant.

Unfortunately, as the pollutant decays, the background atmosphere also evolves, resulting in a chemical mixture after 30 days that differs greatly from the initial ATom free troposphere. The observed free tropospheric composition is maintained by several non-local processes that are not included in our box model (e.g., lightning NO_x, convective mixing of surface pollution, washout scavenging, injection of stratospheric O_3). Thus, in our F0AM box model we introduce artificial sources or sinks to maintain a stable composition (see Table 7). These artificial terms are derived for the major free-troposphere species at each level with an iterative sequence. First, we fixed the concentrations of the controlled species (NO_x, O_3, CO, H_2O_2, ethane, propane, *n*-butane, benzene, toluene, acetone) and integrate the full chemistry for 30 days, allowing the numerous short-lived secondary species to achieve some balance. For controlled species with daily net losses, we add an artificial source to match the loss. For those with excess production, we estimate a first-order loss to balance it. Applying these artificial source/sink terms, we run a 365-day constant-summertime spin-up with primary species evolving. We rescale the source/sink terms by the ratio of the initial-to-final concentrations. This process is iterated, with some Aitken acceleration for O_3, until the end-of-year concentrations differ by less than 1% from the initial ATom values (Table 2). This provides a stable chemical composition upon which to integrate the impact of decaying pollutants.

The DP stage F0AM calculations are integrated as for the PL stage (*i.e.*, constant meteorology, 30 min SZA timestepping, fixed CH_4 and water vapour, and KORUS-AQ all-sky *J*-values sampled above 1.5 km) for the four altitude bins in Table 2. For each pollutant, we follow the decay of a small enhancement (+0.1 ppb) on the four altitude levels for 30 days. We then collect the remaining moles of pollutant and secondary products (e.g., CO from VOCs) from the four levels, mix them and redistribute again across the four levels (Table 2). This 30-day timescale for mixing is consistent with the vertical age gradients of 3-4 days per km found in 3D models (Prather 2025, Fig. 9). We repeat this sequence (age 30 days and then mix across levels) three times for 120 days total, effectively oxidizing most all of the original and secondary pollutants. The vertical mixing is needed to allow the total pollution to decay because the chemical loss of several species is extremely slow if left in the upper troposphere.

For each perturbation by pollutant X, we calculate this 120-day sequence and compare with a reference run made without added pollution. For CH_4 loss (total in ppb), we sum the OH+CH_4 reaction rate for pollution minus control runs. With CH_4 fixed in our model, this directly gives us the pollution-driven net loss. For O_3, the diagnosis of net production is more difficult because the chemistry both produces and destroys O_3 on a time scale of weeks. The use of odd-oxygen production rates to represent O_3 production is fundamentally flawed because these rates depend on the O_3 abundance (see, Guo et al., 2023; Prather & Zhu, 2024). Thus, we use the integral of the O_3 perturbation (ppb days) at each altitude over the 120-day DP integration and divide by the O_3 perturbation lifetime (days) for that altitude. Provided that the O_3 perturbation has fully decayed, this quotient is exactly the net O_3 produced (ppb). For proof, see Prather (2007). The O_3 perturbation lifetime given in Table 7 at each altitude is a well-determined, well-defined value since it is derived from a pulsed O_3 addition and integrated

https://doi.org/10.5194/egusphere-2025-6012
Preprint. Discussion started: 5 December 2025

for 120 days (without vertical mixing). With vertical mixing every 30 days, our derivation of net O_3 production is only approximate because we do not follow the perturbation from beginning to end under a single chemistry. For the most part, the O_3 perturbation from pollutant X occurs at the beginning of the 30 days and decays by the end. We do not tabulate the O_3 perturbation caused by an O_3 pollutant since that would be double counting, but we do calculate the CH_4 perturbation caused by O_3.

The O_3 perturbation lifetime at 2 km altitude (5.8 days) is used to calculate the PL stage net production by accounting for the limited decay over 1-3 days. For the DP stage we can simply divide the integrated perturbation (ppb-days) by lifetime (days) to net production (ppb). We rescale these net reactivities by the amount of primary pollutant X used in the calculation to derive dCH_4/dX and dO_3/dX in mol mol^{-1}. The total impact of all pollution released to the DP stage (see Fig. 7) is given in Table 8. We find that PAN and peroxypropionyl nitrate (PPN) produce similar dCH_4/dX and dO_3/dX reactivity values to NO_2 and NO, and hence we apply the reactivities of NO_2 to all peroxyacyl, alkyl, and aromatic nitrates that we did not calculate explicitly.

Table 7: Dispersed plume model parameters and resulting O_3 lifetime

Species	**Source, molec cm^{-3} s^{-1} (Sink, s^{-1})**			
	2 km	**4 km**	**6 km**	**8 km**
NO	19500	8190	5810	3780
NO_2	0	0	0	0
CO	808000	421000	251000	143000
Ethane	14200	6440	2970	1300
Propane	3690	1570	634	533
n-Butane	711	297	183	139
n-Pentane	0	0	0	0
Acetone	2770	2320	1790	1340
Benzene	1410	473	255	184
Toluene	117	36	37	29
O_3	586000	212000	43500	(8.35E-08)
H_2O_2	(2.60E-05)	(6.84E-06)	(3.96E-06)	(8.20E-07)

https://doi.org/10.5194/egusphere-2025-6012
Preprint. Discussion started: 5 December 2025

O_3 perturbation lifetime (days)	5.8	10.8	17.9	24.2

Sources (molec cm^{-3} s^{-1}) and sinks (s^{-1}) represent the atmospheric processes that maintain a quasi-steady-state for each species for the ATom background atmosphere adopted here. The O_3 lifetimes are derived from the decay of a unit O_3 perturbation at each altitude. Methyl hydroperoxide, which was not constrained in the DP stage, equilibrated at 0.42, 0.30, 0.16, and 0.06 ppb in the altitude bins from 2 to 8 km compared with 0.71, 0.55, 0.40, and 0.23 ppb observed in ATom, consistent with the long-standing view that convection of BL CH_3OOH (not included here) provides a major FT source (Prather and Jacob, 1997).

Table 8: CH_4 and O_3 budget perturbations in the DP stage from the more important individual pollutants.

Pollutant	**Emissions (Gmol)**	**Dispersed (Gmol)**	**ΔCH_4 (Gmol)**	**ΔO_3 (Gmol)**
CO	7.3	7.0	+2.8	+1.6
O_3	N/A	14.4	-1.8	0
PAN	N/A	0.17	-1.9	+5.1
NO_x	3.5	0.04	-0.4	+1.2
Other peroxyacyl nitrates	N/A	0.05	-0.5	+1.4
Alkyl nitrates	N/A	0.02	-0.2	+0.6
Aromatic nitrates	N/A	0.02	-0.2	+0.6
Benzene	0.1	0.04	-0.0	+0.2
Toluene	0.3	-0.01	-0.1	-0.1

"Emissions" includes 45 days of anthropogenic South Korean emissions (KORUS v5 + GFED5). "Dispersed" values are the pollution remnants after BL-RL processing and 3 days of aging in the PL stage. ΔCH_4 and ΔO_3 are the budget perturbations caused by individual pollutants in the DP stage, and are proportional to the moles of dispersing pollutants. "Dispersed" negative toluene is caused by chemical loss of toluene in entrained FT air that exceeds emissions.

4 Ozone and methane budgets

We calculate the impact of South Korean pollution on O_3 and CH_4 by differencing a full emission run and a reference control run without KORUS v5 anthropogenic and GFED5 biomass burning emissions. Our assessment is for the 45 days of emissions (02 May to 15 June 2016) covering the KORUS-AQ mission in South Korea. We follow 2 spin-down days (16-17 June 2016) without industrial or biomass burning emissions to account for the 45 days of pollution leaving the peninsula. We calculate

https://doi.org/10.5194/egusphere-2025-6012
Preprint. Discussion started: 5 December 2025

the budget terms (Gmol) for O_3 and CH_4 directly from all BL, RL, and PL air masses, and then add on DP stage by scaling the dO_3/dX and dCH_4/dX factors by the amount of each pollutant X (Gmol) released into the free troposphere.

Following the O_3 budget requires careful accounting. The change in O_3 during the BL-RL stage relative to the control occurs on the order of one day and is almost a direct measure of the net production (loss). Over that time, the net production will decay. The average residence time for dry air in the BL-RL model is 8 hr (mean South Korean BL+RL mass per daily offshore export), but for chemically-produced O_3, it is 12 hr. Based on Table 7, we select 4.5 days as the BL-RL O_3 perturbation lifetime at 1 km altitude, and thus, net production of O_3 occurring uniformly across 12 hr will decay on average by over 5.4% by the end of the day. We multiply the BL-RL O_3 perturbation that is put into the PL stage by the reciprocal decay (1.06) to estimate net BL-RL production. The BL-RL stage often produces large net losses from cells with high NO_x emissions, and we assume these perturbations also decay with the 4.5-day timescale. Our method of extracting net BL-RL O_3 production is only approximate because the O_3 perturbation lifetime is likely variable depending on chemical regimes, and the time spent by pollution in the BL-RL model can vary from hours up to 2 days.

Deriving the net O_3 production from the PL stage is more straightforward. There are three successive 24-hour days of plume chemistry integration, occurring under the same atmospheric conditions (2 km) but under different chemical conditions. We do not attempt to derive the O_3 lifetime for each PL case, but make the approximation that it is the same as the free troposphere in the 2 km DP case (5.8 days). At the start of each PL day, we have an O_3 perturbation that is carried forward from the previous day: for day 0 it is the O_3 perturbation from the BL-RL masses that collected in the plume; for days 1-to-3 it is the perturbation at the end of the previous day relative to the control. We assume that this external O_3 perturbation decays with a 5.8-day lifetime (i.e., 16% day^{-1}). The net internal O_3 perturbation at the end of the day caused by the PL chemistry is then the O_3 at the end of the day minus the decayed residual of the external perturbation from the beginning of the day relative to the control run. Because of decay over the 24-hour plume integration, the net internal perturbation is increased by 9% to get the net production. This complex sequence allows us to account for the effective net O_3 production over the PL stage without double counting. When we integrate the impact of an O_3 perturbation passed on to the DP stage, the integral of CH_4 reactivity is straightforward and must be included, but the integral of the O_3 perturbation itself cannot be included since its net production was already accounted for in the previous stages.

The total CH_4 and O_3 reactivities attributed to the 45 days of emissions are -4.3 Gmol and +31.3 Gmol, respectively, for 3-day plume lifetime (see Table 9). For both species, 85% of the reactivity occurs during the 45-day emission period, and the remaining 15% occurs over the following 2 months (see supplemental Fig. S8 for reactivity timeline). Table 9 shows the budget terms during the individual model stages, the ozone enhancements that resulted from production, and the ozone production efficiencies (OPE = molar production of O_3 per molar loss of NO_x). Methane and O_3 reactivity occurs mostly in the PL and DP stages, wherein the total budgets are highly responsive to aging time in the plumes (PL stage). Our standard diagnostics are for 3-day plumes, and reducing this lifetime results in much larger reactivities. Varying the plume aging time from 3 days to 2 days results in the addition of -0.5 Gmol-CH_4 and +1.9 Gmol-O_3 to the budgets. Varying from 2-to-1 days results in -1.0 Gmol-CH_4, and +2.7 Gmol-O_3, and from 1-to-0 days, -8.3 Gmol-CH_4 and +20.5 Gmol-O_3. The range of

https://doi.org/10.5194/egusphere-2025-6012
Preprint. Discussion started: 5 December 2025

reactivities from instant dilution to infinite aging is 11 Gmol-CH_4 and 31 Gmol-O_3 assuming geometric convergence with a common ratio of 1/2. Hence, the change in reactivities from 3-to-2 days aging in plumes accounts for just 5% of the possible range of reactivities, with 10% from 2-to-1 days, and 75% from 1-to-0 days. The true timescales of pollution plume dilution are presently unknown but likely on the order of a few days. Global models commonly dilute pollution plumes too rapidly (Zhuang *et al*., 2018), and could vastly overestimate the O_3 and CH_4 budget contributions from anthropogenic pollution as a result.

The OPEs in our model stages are diagnosed from the tabulated O_3 production and the loss of reactive nitrogen (NO_x, NO_3, $2N_2O_5$, HO_2NO_2, HONO, PAN and other peroxyacyl nitrates, alkyl nitrates, and aromatic nitrates) (not shown). The BL-RL and PL stage OPEs are consistent with Oak *et al*. (2019) urban South Korean BL OPEs and box modelled DC-8 OPEs that were diagnosed from instantaneous NO_2 formation, odd-oxygen loss, and NO_2-OH oxidation rates. Since half of our NO_x-loss comes from nocturnal N_2O_5 aerosol reactivity, our OPEs are halved compared with Oak *et al*. (2019). The DP stage OPE diagnosed from pure NO_x dispersion follows the classic non-linear response to NO_x levels (Liu *et al*., 1987) and is close to the OPE from aviation NO_x (31 mol mol^{-1}; Prather and Zhu, 2024).

Table 9: Total CH_4 and O_3 budget perturbations and OPE over 45 days of South Korean air pollution.

Model stage	CH_4 reactivity (Gmol)	O_3 reactivity (Gmol)	O_3 perturbation (Gmol days)	OPE (Gmol $Gmol^{-1}$)
BL-RL	-0.3	+4.0	1.8	2.3
3-day PL	-1.7	+16.3	33.9	11.2
DP (3-day PL)	-2.3	+10.9	284	27.8
Total (3-day PL)	-4.3	+31.2	320	8.9
Total (2-day PL)	-4.8	+33.1	351	-
Total (1-day PL)	-5.8	+35.8	389	-
Total (0-day PL)	-14.1	+59.0	687	-
Total (emissions directly to DP)	-30.1	+103.2	1250	-

CH_4 and O_3 reactivities are net productions (negative = loss) summed over the individual modelling stages, and as totals for all stages given varying plume aging times. O_3 perturbations are the integrated enhancements of O_3 (Gmol) summed during the stages, and as model totals. Ozone production efficiency (OPE) is computed as the net O_3 production (i.e., "O_3 reactivity") per NO_y-nitrogen loss (mol mol^{-1}) over several stages, or in total. The DP stage OPE excludes secondary NO_y perturbations from dispersing VOCs.

https://doi.org/10.5194/egusphere-2025-6012
Preprint. Discussion started: 5 December 2025

5 Conclusion

Our modelling system calculates the tropospheric OH-loss of CH_4 and the net production of O_3 from South Korean air pollution during the May-June 2016 KORUS-AQ period. Methane loss is diagnosed from CH_4+OH rate in all three modelling stages, from boundary layer to plumes to the ultimate dispersion in the free troposphere. Ozone production is inferred through the integrated O_3 perturbation (*i.e.*, mole-days) and our calculation of the O_3 perturbation lifetimes (*i.e.*, days). This use of a perturbation lifetime to derive the effective "emission" of O_3 is necessary because the typical modelling approach of using the odd-oxygen rates (e.g., Griffiths et al., 2021) fails to account for the feedbacks of O_3 on the production of odd-oxygen as discussed in Prather and Zhu (2024).

The total perturbations to CH_4 and O_3 caused by 45 days of South Korean air pollution are -4.3 Gmol and +31.3 Gmol respectively. The global annual tropospheric CH_4 loss for this period is about 35,200 Gmol (Saunois *et al*., 2025), and hence the 45-day global loss is 4,300 Gmol. The tropospheric O_3 budget is more complex than the CH_4 budget, but if we take a simple estimate from the models reporting odd-oxygen rates in Griffiths et al. (2021), we have a mean tropospheric burden of 7020 Gmol (337 Tg-O_3) and a production time of 27 days. Thus, the global reactivity for the 45-day KORUS period is -4,300 Gmol CH_4 and +11,700 Gmol O_3. We estimate the South Korean NO_x emissions to be of order 1% of global anthropogenic emissions (Hoesly et al., 2018), and scaling this gives 10% of total CH_4 loss and 27% of total O_3 production attributable to anthropogenic pollution. Our scaling estimates are simplistic and biased high because the reactivity of pollution depends greatly on latitude and season. The KORUS-AQ campaign was during a period of greatest photochemical activity. Unfortunately, we do not have the data sets and capability to repeat this study with the full annual cycle of Korean pollution.

The O_3 and CH_4 reactivities are highly sensitive to the aging of pollution in plumes. If the plumes disperse to the free troposphere immediately (0-day PL in Table 9), the total reactivities approximately double our standard estimates for 3-day aging. Typically, global models fail to preserve interior plume concentrations beyond a few days at best due to numerical diffusion (Zhuang *et al.*, 2018). The inability to maintain pollution in large-scale plumes is probably one of the larger sources of error in CTMs, and the community would benefit from observational studies on pollution plume dynamics to establish the typical timescales of mixing into the free troposphere.

Code and Data availability

All KORUS-AQ data used in this paper are available via https://doi.org/10.5067/Suborbital/KORUSAQ/DATA01 (KORUS-AQ Science Team, 2019). Model code and datasets for analysis are available via Wilson, 2025.

Author contributions

CPW co-designed the modelling system, wrote the model code, performed the analysis, and co-wrote the manuscript. MJP strategised the modelling study, co-designed the modelling system, and co-wrote the manuscript.

https://doi.org/10.5194/egusphere-2025-6012
Preprint. Discussion started: 5 December 2025

Competing interests

The contact author has declared that neither of the authors has any competing interests.

Acknowledgements

We acknowledge the European Centre for Medium-Range Weather Forecasts for providing the meteorology used in our study, and NASA, for providing the trace gas data.

Financial support

This research has been supported by the National Aeronautics and Space Administration (grant no. 80NSSC21K1454) and the National Science Foundation (grant no. AGS-2135749).

7 References

Bi, C.; Isaacman-VanWertz, G. Estimated Timescales for Wet Deposition of Organic Compounds as a Function of Henry's Law Constants. Environmental Science: Atmospheres 2022, 2 (6), 1526–1533. https://doi.org/10.1039/D2EA00091A.

Bloss, C.; Wagner, V.; Jenkin, M. E.; Volkamer, R.; Bloss, W. J.; Lee, J. D.; Heard, D. E.; Wirtz, K.; Martin-Reviejo, M.; Rea, G.; Wenger, J. C.; Pilling, M. J. Development of a Detailed Chemical Mechanism (MCMv3.1) for the Atmospheric Oxidation of Aromatic Hydrocarbons. Atmospheric Chemistry and Physics 2005, 5 (3), 641–664. https://doi.org/10.5194/acp-5-641-2005.

Bourgeois, I.; Peischl, J.; Thompson, C. R.; Aikin, K. C.; Campos, T.; Clark, H.; Commane, R.; Daube, B.; Diskin, G. W.; Elkins, J. W.; Gao, R.-S.; Gaudel, A.; Hintsa, E. J.; Johnson, B. J.; Kivi, R.; McKain, K.; Moore, F. L.; Parrish, D. D.; Querel, R.; Ray, E.; Sánchez, R.; Sweeney, C.; Tarasick, D. W.; Thompson, A. M.; Thouret, V.; Witte, J. C.; Wofsy, S. C.; Ryerson, T. B. Global-Scale Distribution of Ozone in the Remote Troposphere from the ATom and HIPPO Airborne Field Missions. Atmospheric Chemistry and Physics 2020, 20 (17), 10611–10635. https://doi.org/10.5194/acp-20-10611-2020.

Brook, J. R.; Zhang, L.; Li, Y.; Johnson, D. Description and Evaluation of a Model of Deposition Velocities for Routine Estimates of Dry Deposition over North America. Part II: Review of Past Measurements and Model Results. Atmospheric Environment 1999, 33 (30), 5053–5070. https://doi.org/10.1016/S1352-2310(99)00251-4.

https://doi.org/10.5194/egusphere-2025-6012
Preprint. Discussion started: 5 December 2025

Carter, W. P. L. Development of the SAPRC-07 Chemical Mechanism. Atmospheric Environment 2010, 44 (40), 5324–5335. https://doi.org/10.1016/j.atmosenv.2010.01.026.

Chen, Y.; Hall, J.; van Wees, D.; Andela, N.; Hantson, S.; Giglio, L.; van der Werf, G. R.; Morton, D. C.; Randerson, J. T. Multi-Decadal Trends and Variability in Burned Area from the Fifth Version of the Global Fire Emissions Database (GFED5). Earth System Science Data 2023, 15 (11), 5227–5259. https://doi.org/10.5194/essd-15-5227-2023.

Cho, C.; Clair, J. M. St.; Liao, J.; Wolfe, G. M.; Jeong, S.; Kang, D. il; Choi, J.; Shin, M.-H.; Park, J.; Park, J.-H.; Fried, A.; Weinheimer, A.; Blake, D. R.; Diskin, G. S.; Ullmann, K.; Hall, S. R.; Brune, W. H.; Hanisco, T. F.; Min, K.-E. Evolution of Formaldehyde (HCHO) in a Plume Originating from a Petrochemical Industry and Its Volatile Organic Compounds (VOCs) Emission Rate Estimation. Elementa: Science of the Anthropocene 2021, 9 (1), 00015. https://doi.org/10.1525/elementa.2021.00015.

Crawford, J. H.; Heald, C. L.; Fuelberg, H. E.; Morse, D. M.; Sachse, G. W.; Emmons, L. K.; Gille, J. C.; Edward, D. P.; Deeter, M. N.; Chen, G.; Olson, J. R.; Connors, V. S.; Kittaka, C.; Hamlin, A. J. Relationship between Measurements of Pollution in the Troposphere (MOPITT) and in Situ Observations of CO Based on a Large-Scale Feature Sampled during TRACE-P. Journal of Geophysical Research: Atmospheres 2004, 109 (D15). https://doi.org/10.1029/2003JD004308.

Crawford, J. H.; Ahn, J.-Y.; Al-Saadi, J.; Chang, L.; Emmons, L. K.; Kim, J.; Lee, G.; Park, J.-H.; Park, R. J.; Woo, J. H.; Song, C.-K.; Hong, J.-H.; Hong, Y.-D.; Lefer, B. L.; Lee, M.; Lee, T.; Kim, S.; Min, K.-E.; Yum, S. S.; Shin, H. J.; Kim, Y.-W.; Choi, J.-S.; Park, J.-S.; Szykman, J. J.; Long, R. W.; Jordan, C. E.; Simpson, I. J.; Fried, A.; Dibb, J. E.; Cho, S.; Kim, Y. P. The Korea–United States Air Quality (KORUS-AQ) Field Study. Elementa: Science of the Anthropocene 2021, 9 (1), 00163. https://doi.org/10.1525/elementa.2020.00163.

Crippa, M.; Solazzo, E.; Huang, G.; Guizzardi, D.; Koffi, E.; Muntean, M.; Schieberle, C.; Friedrich, R.; Janssens-Maenhout, G. High Resolution Temporal Profiles in the Emissions Database for Global Atmospheric Research. Sci Data 2020, 7 (1), 121. https://doi.org/10.1038/s41597-020-0462-2.

de Gouw, J. A.; Gilman, J. B.; Kim, S.-W.; Lerner, B. M.; Isaacman-VanWertz, G.; McDonald, B. C.; Warneke, C.; Kuster, W. C.; Lefer, B. L.; Griffith, S. M.; Dusanter, S.; Stevens, P. S.; Stutz, J. Chemistry of Volatile Organic Compounds in the Los Angeles Basin: Nighttime Removal of Alkenes and Determination of Emission Ratios. Journal of Geophysical Research: Atmospheres 2017, 122 (21), 11,843-11,861. https://doi.org/10.1002/2017JD027459.

https://doi.org/10.5194/egusphere-2025-6012
Preprint. Discussion started: 5 December 2025

Eck, T. F.; Holben, B. N.; Kim, J.; Beyersdorf, A. J.; Choi, M.; Lee, S.; Koo, J.-H.; Giles, D. M.; Schafer, J. S.; Sinyuk, A.; Peterson, D. A.; Reid, J. S.; Arola, A.; Slutsker, I.; Smirnov, A.; Sorokin, M.; Kraft, J.; Crawford, J. H.; Anderson, B. E.; Thornhill, K. L.; Diskin, G.; Kim, S.-W.; Park, S. Influence of Cloud, Fog, and High Relative Humidity during Pollution Transport Events in South Korea: Aerosol Properties and PM2.5 Variability. Atmospheric Environment 2020, 232, 117530. https://doi.org/10.1016/j.atmosenv.2020.117530.

Gaudel, A.; Cooper, O. R.; Ancellet, G.; Barret, B.; Boynard, A.; Burrows, J. P.; Clerbaux, C.; Coheur, P.-F.; Cuesta, J.; Cuevas, E.; Doniki, S.; Dufour, G.; Ebojie, F.; Foret, G.; Garcia, O.; Granados-Muñoz, M. J.; Hannigan, J. W.; Hase, F.; Hassler, B.; Huang, G.; Hurtmans, D.; Jaffe, D.; Jones, N.; Kalabokas, P.; Kerridge, B.; Kulawik, S.; Latter, B.; Leblanc, T.; Le Flochmoën, E.; Lin, W.; Liu, J.; Liu, X.; Mahieu, E.; McClure-Begley, A.; Neu, J. L.; Osman, M.; Palm, M.; Petetin, H.; Petropavlovskikh, I.; Querel, R.; Rahpoe, N.; Rozanov, A.; Schultz, M. G.; Schwab, J.; Siddans, R.; Smale, D.; Steinbacher, M.; Tanimoto, H.; Tarasick, D. W.; Thouret, V.; Thompson, A. M.; Trickl, T.; Weatherhead, E.; Wespes, C.; Worden, H. M.; Vigouroux, C.; Xu, X.; Zeng, G.; Ziemke, J. Tropospheric Ozone Assessment Report: Present-Day Distribution and Trends of Tropospheric Ozone Relevant to Climate and Global Atmospheric Chemistry Model Evaluation. Elementa: Science of the Anthropocene 2018, 6, 39. https://doi.org/10.1525/elementa.291.

Griffiths, P. T.; Murray, L. T.; Zeng, G.; Shin, Y. M.; Abraham, N. L.; Archibald, A. T.; Deushi, M.; Emmons, L. K.; Galbally, I. E.; Hassler, B.; Horowitz, L. W.; Keeble, J.; Liu, J.; Moeini, O.; Naik, V.; O'Connor, F. M.; Oshima, N.; Tarasick, D.; Tilmes, S.; Turnock, S. T.; Wild, O.; Young, P. J.; Zanis, P. Tropospheric Ozone in CMIP6 Simulations. Atmospheric Chemistry and Physics 2021, 21 (5), 4187–4218. https://doi.org/10.5194/acp-21-4187-2021.

Guenther, A. B.; Jiang, X.; Heald, C. L.; Sakulyanontvittaya, T.; Duhl, T.; Emmons, L. K.; Wang, X. The Model of Emissions of Gases and Aerosols from Nature Version 2.1 (MEGAN2.1): An Extended and Updated Framework for Modeling Biogenic Emissions. Geoscientific Model Development 2012, 5 (6), 1471–1492. https://doi.org/10.5194/gmd-5-1471-2012.

Guo, H.; Flynn, C. M.; Prather, M. J.; Strode, S. A.; Steenrod, S. D.; Emmons, L.; Lacey, F.; Lamarque, J.-F.; Fiore, A. M.; Correa, G.; Murray, L. T.; Wolfe, G. M.; St. Clair, J. M.; Kim, M.; Crounse, J.; Diskin, G.; DiGangi, J.; Daube, B. C.; Commane, R.; McKain, K.; Peischl, J.; Ryerson, T. B.; Thompson, C.; Hanisco, T. F.; Blake, D.; Blake, N. J.; Apel, E. C.; Hornbrook, R. S.; Elkins, J. W.; Hintsa, E. J.; Moore, F. L.; Wofsy, S. C. Heterogeneity and Chemical Reactivity of the Remote Troposphere Defined by Aircraft Measurements – Corrected. Atmospheric Chemistry and Physics 2023, 23 (1), 99–117. https://doi.org/10.5194/acp-23-99-2023.

Hall, S. R.; Ullmann, K.; Prather, M. J.; Flynn, C. M.; Murray, L. T.; Fiore, A. M.; Correa, G.; Strode, S. A.; Steenrod, S. D.; Lamarque, J.-F.; Guth, J.; Josse, B.; Flemming, J.; Huijnen, V.; Abraham, N. L.; Archibald, A. T. Cloud Impacts on

https://doi.org/10.5194/egusphere-2025-6012
Preprint. Discussion started: 5 December 2025

Photochemistry: Building a Climatology of Photolysis Rates from the Atmospheric Tomography Mission. Atmospheric Chemistry and Physics 2018, 18 (22), 16809–16828. https://doi.org/10.5194/acp-18-16809-2018.

Heald, C. L.; Jacob, D. J.; Jones, D. B. A.; Palmer, P. I.; Logan, J. A.; Streets, D. G.; Sachse, G. W.; Gille, J. C.; Hoffman, R. N.; Nehrkorn, T. Comparative Inverse Analysis of Satellite (MOPITT) and Aircraft (TRACE-P) Observations to Estimate Asian Sources of Carbon Monoxide. Journal of Geophysical Research: Atmospheres 2004, 109 (D23). https://doi.org/10.1029/2004JD005185.

Hersbach, H., Bell, B., Berrisford, P., Hirahara, S., Horányi, A., Muñoz-Sabater, J., Nicolas, J., Peubey, C., Radu, R., Schepers, D., Simmons, A., Soci, C., Abdalla, S., Abellan, X., Balsamo, G., Bechtold, P., Biavati, G., Bidlot, J., Bonavita, M., De Chiara, G., Dahlgren, P., Dee, D., Diamantakis, M., Dragani, R., Flemming, J., Forbes, R., Fuentes, M., Geer, A., Haimberger, L., Healy, S., Hogan, R.J., Hólm, E., Janisková, M., Keeley, S., Laloyaux, P., Lopez, P., Lupu, C., Radnoti, G., de Rosnay, P., Rozum, I., Vamborg, F., Villaume, S., Thépaut, J-N. (2017): Complete ERA5 from 1940: Fifth generation of ECMWF atmospheric reanalyses of the global climate. Copernicus Climate Change Service (C3S) Data Store (CDS) [data set]. DOI: 10.24381/cds.143582cf (Accessed on 17-Jun-2025)

Hersbach, H., Bell, B., Berrisford, P., Biavati, G., Horányi, A., Muñoz Sabater, J., Nicolas, J., Peubey, C., Radu, R., Rozum, I., Schepers, D., Simmons, A., Soci, C., Dee, D., Thépaut, J-N. (2023): ERA5 hourly data on single levels from 1940 to present. Copernicus Climate Change Service (C3S) Climate Data Store (CDS), DOI: 10.24381/cds.adbb2d47 (Accessed on 26-Feb-2025)

Hsu, J.; Prather, M. J.; Wild, O.; Sundet, J. K.; Isaksen, I. S. A.; Browell, E. V.; Avery, M. A.; Sachse, G. W. Are the TRACE-P Measurements Representative of the Western Pacific during March 2001? Journal of Geophysical Research: Atmospheres 2004, 109 (D2). https://doi.org/10.1029/2003JD004002.

Isaksen, I. S. A.; Hov, Ø. Calculation of Trends in the Tropospheric Concentration of O3, OH, CO, CH4 and NOx | Tellus B: Chemical and Physical Meteorology. 2022. https://doi.org/10.3402/tellusb.v39i3.15347.

Jacob, D. J.; Crawford, J. H.; Kleb, M. M.; Connors, V. S.; Bendura, R. J.; Raper, J. L.; Sachse, G. W.; Gille, J. C.; Emmons, L.; Heald, C. L. Transport and Chemical Evolution over the Pacific (TRACE-P) Aircraft Mission: Design, Execution, and First Results. Journal of Geophysical Research: Atmospheres 2003, 108 (D20). https://doi.org/10.1029/2002JD003276.

Jenkin, M. E.; Saunders, S. M.; Pilling, M. J. The Tropospheric Degradation of Volatile Organic Compounds: A Protocol for Mechanism Development. Atmospheric Environment 1997, 31 (1), 81–104. https://doi.org/10.1016/S1352-2310(96)00105-7.

https://doi.org/10.5194/egusphere-2025-6012
Preprint. Discussion started: 5 December 2025

Jenkin, M. E.; Saunders, S. M.; Wagner, V.; Pilling, M. J. Protocol for the Development of the Master Chemical Mechanism, MCM v3 (Part B): Tropospheric Degradation of Aromatic Volatile Organic Compounds. Atmospheric Chemistry and Physics 2003, 3 (1), 181–193. https://doi.org/10.5194/acp-3-181-2003.

Jenkin, M. E.; Young, J. C.; Rickard, A. R. The MCM v3.3.1 Degradation Scheme for Isoprene. Atmospheric Chemistry and Physics 2015, 15 (20), 11433–11459. https://doi.org/10.5194/acp-15-11433-2015.

Jia, Y.; Yu, G.; Gao, Y.; He, N.; Wang, Q.; Jiao, C.; Zuo, Y. Global Inorganic Nitrogen Dry Deposition Inferred from Ground- and Space-Based Measurements. Sci Rep 2016, 6 (1), 19810. https://doi.org/10.1038/srep19810.

Jung, J.; Lee, J.; Kim, B.; Oh, S. Seasonal Variations in the NO2 Artifact from Chemiluminescence Measurements with a Molybdenum Converter at a Suburban Site in Korea (Downwind of the Asian Continental Outflow) during 2015–2016. Atmospheric Environment 2017, 165, 290–300. https://doi.org/10.1016/j.atmosenv.2017.07.010.

Kim, K.-M.; Kim, S.-W.; Seo, S.; Blake, D. R.; Cho, S.; Crawford, J. H.; Emmons, L. K.; Fried, A.; Herman, J. R.; Hong, J.; Jung, J.; Pfister, G. G.; Weinheimer, A. J.; Woo, J.-H.; Zhang, Q. Sensitivity of the WRF-Chem v4.4 Simulations of Ozone and Formaldehyde and Their Precursors to Multiple Bottom-up Emission Inventories over East Asia during the KORUS-AQ 2016 Field Campaign. Geoscientific Model Development 2024, 17 (4), 1931–1955. https://doi.org/10.5194/gmd-17-1931-2024.

KORUS-AQ Science Team: KORUS-AQ NASA DC-8 airborne 10 s merged data revision 6 - ICARTT Files, NASA Langley Atmospheric Science Data Center DAAC [data set], https://doi.org/10.5067/Suborbital/KORUSAQ/DATA01, 2019.

Lamarque, J.-F.; Emmons, L. K.; Hess, P. G.; Kinnison, D. E.; Tilmes, S.; Vitt, F.; Heald, C. L.; Holland, E. A.; Lauritzen, P. H.; Neu, J.; Orlando, J. J.; Rasch, P. J.; Tyndall, G. K. CAM-Chem: Description and Evaluation of Interactive Atmospheric Chemistry in the Community Earth System Model. Geoscientific Model Development 2012, 5 (2), 369–411. https://doi.org/10.5194/gmd-5-369-2012.

Lee, Y. R.; Huey, L. G.; Tanner, D. J.; Takeuchi, M.; Qu, H.; Liu, X.; Ng, N. L.; Crawford, J. H.; Fried, A.; Richter, D.; Simpson, I. J.; Blake, D. R.; Blake, N. J.; Meinardi, S.; Kim, S.; Diskin, G. S.; Digangi, J. P.; Choi, Y.; Pusede, S. E.; Wennberg, P. O.; Kim, M. J.; Crounse, J. D.; Teng, A. P.; Cohen, R. C.; Romer, P. S.; Brune, W.; Wisthaler, A.; Mikoviny, T.; Jimenez, J. L.; Campuzano-Jost, P.; Nault, B. A.; Weinheimer, A.; Hall, S. R.; Ullmann, K. An Investigation of Petrochemical Emissions

https://doi.org/10.5194/egusphere-2025-6012
Preprint. Discussion started: 5 December 2025

during KORUS-AQ: Ozone Production, Reactive Nitrogen Evolution, and Aerosol Production. Elementa: Science of the Anthropocene 2022, 10 (1), 00079. https://doi.org/10.1525/elementa.2022.00079.

Liang, Q.; Jaeglé, L.; Hudman, R. C.; Turquety, S.; Jacob, D. J.; Avery, M. A.; Browell, E. V.; Sachse, G. W.; Blake, D. R.; Brune, W.; Ren, X.; Cohen, R. C.; Dibb, J. E.; Fried, A.; Fuelberg, H.; Porter, M.; Heikes, B. G.; Huey, G.; Singh, H. B.; Wennberg, P. O. Summertime Influence of Asian Pollution in the Free Troposphere over North America. Journal of Geophysical Research: Atmospheres 2007, 112 (D12). https://doi.org/10.1029/2006JD007919.

Lin, X.; Trainer, M.; Liu, S. C. On the Nonlinearity of the Tropospheric Ozone Production. Journal of Geophysical Research: Atmospheres 1988, 93 (D12), 15879–15888. https://doi.org/10.1029/JD093iD12p15879.

Miyazaki, K.; Sekiya, T.; Fu, D.; Bowman, K. W.; Kulawik, S. S.; Sudo, K.; Walker, T.; Kanaya, Y.; Takigawa, M.; Ogochi, K.; Eskes, H.; Boersma, K. F.; Thompson, A. M.; Gaubert, B.; Barre, J.; Emmons, L. K. Balance of Emission and Dynamical Controls on Ozone During the Korea-United States Air Quality Campaign From Multiconstituent Satellite Data Assimilation. Journal of Geophysical Research: Atmospheres 2019, 124 (1), 387–413. https://doi.org/10.1029/2018JD028912.

Nault, B. A.; Campuzano-Jost, P.; Day, D. A.; Schroder, J. C.; Anderson, B.; Beyersdorf, A. J.; Blake, D. R.; Brune, W. H.; Choi, Y.; Corr, C. A.; de Gouw, J. A.; Dibb, J.; DiGangi, J. P.; Diskin, G. S.; Fried, A.; Huey, L. G.; Kim, M. J.; Knote, C. J.; Lamb, K. D.; Lee, T.; Park, T.; Pusede, S. E.; Scheuer, E.; Thornhill, K. L.; Woo, J.-H.; Jimenez, J. L. Secondary Organic Aerosol Production from Local Emissions Dominates the Organic Aerosol Budget over Seoul, South Korea, during KORUS-AQ. Atmospheric Chemistry and Physics 2018, 18 (24), 17769–17800. https://doi.org/10.5194/acp-18-17769-2018.

Park, R. J.; Oak, Y. J.; Emmons, L. K.; Kim, C.-H.; Pfister, G. G.; Carmichael, G. R.; Saide, P. E.; Cho, S.-Y.; Kim, S.; Woo, J.-H.; Crawford, J. H.; Gaubert, B.; Lee, H.-J.; Park, S.-Y.; Jo, Y.-J.; Gao, M.; Tang, B.; Stanier, C. O.; Shin, S. S.; Park, H. Y.; Bae, C.; Kim, E. Multi-Model Intercomparisons of Air Quality Simulations for the KORUS-AQ Campaign. Elementa: Science of the Anthropocene 2021, 9 (1), 00139. https://doi.org/10.1525/elementa.2021.00139.

Peterson, D. A.; Hyer, E. J.; Han, S.-O.; Crawford, J. H.; Park, R. J.; Holz, R.; Kuehn, R. E.; Eloranta, E.; Knote, C.; Jordan, C. E.; Lefer, B. L. Meteorology Influencing Springtime Air Quality, Pollution Transport, and Visibility in Korea. Elementa: Science of the Anthropocene 2019, 7, 57. https://doi.org/10.1525/elementa.395.

Prather, M. J. Lifetimes and Time Scales in Atmospheric Chemistry. Philosophical Transactions of the Royal Society A: Mathematical, Physical and Engineering Sciences 2007, 365 (1856), 1705–1726. https://doi.org/10.1098/rsta.2007.2040.

https://doi.org/10.5194/egusphere-2025-6012
Preprint. Discussion started: 5 December 2025

820 Prather, M. J.; Guo, H.; Zhu, X. Deconstruction of Tropospheric Chemical Reactivity Using Aircraft Measurements: The Atmospheric Tomography Mission (ATom) Data. Earth System Science Data 2023, 15 (7), 3299–3349. https://doi.org/10.5194/essd-15-3299-2023.

Prather, M. J.; Zhu, X. Lifetimes and Timescales of Tropospheric Ozone. Elementa: Science of the Anthropocene 2024, 12
825 (1), 00112. https://doi.org/10.1525/elementa.2023.00112.

Prather, M. J. Calibrating the Tropospheric Air and Ozone Mass. AGU Advances 2025, 6 (3), e2025AV001651. https://doi.org/10.1029/2025AV001651.

830 Saunders, S. M.; Jenkin, M. E.; Derwent, R. G.; Pilling, M. J. Protocol for the Development of the Master Chemical Mechanism, MCM v3 (Part A): Tropospheric Degradation of Non-Aromatic Volatile Organic Compounds. Atmospheric Chemistry and Physics 2003, 3 (1), 161–180. https://doi.org/10.5194/acp-3-161-2003.

Saunois, M.; Martinez, A.; Poulter, B.; Zhang, Z.; Raymond, P. A.; Regnier, P.; Canadell, J. G.; Jackson, R. B.; Patra, P. K.;
835 Bousquet, P.; Ciais, P.; Dlugokencky, E. J.; Lan, X.; Allen, G. H.; Bastviken, D.; Beerling, D. J.; Belikov, D. A.; Blake, D. R.; Castaldi, S.; Crippa, M.; Deemer, B. R.; Dennison, F.; Etiope, G.; Gedney, N.; Höglund-Isaksson, L.; Holgerson, M. A.; Hopcroft, P. O.; Hugelius, G.; Ito, A.; Jain, A. K.; Janardanan, R.; Johnson, M. S.; Kleinen, T.; Krummel, P. B.; Lauerwald, R.; Li, T.; Liu, X.; McDonald, K. C.; Melton, J. R.; Mühle, J.; Müller, J.; Murguia-Flores, F.; Niwa, Y.; Noce, S.; Pan, S.; Parker, R. J.; Peng, C.; Ramonet, M.; Riley, W. J.; Rocher-Ros, G.; Rosentreter, J. A.; Sasakawa, M.; Segers, A.; Smith, S. J.;
840 Stanley, E. H.; Thanwerdas, J.; Tian, H.; Tsuruta, A.; Tubiello, F. N.; Weber, T. S.; van der Werf, G. R.; Worthy, D. E. J.; Xi, Y.; Yoshida, Y.; Zhang, W.; Zheng, B.; Zhu, Q.; Zhu, Q.; Zhuang, Q. Global Methane Budget 2000–2020. Earth System Science Data 2025, 17 (5), 1873–1958. https://doi.org/10.5194/essd-17-1873-2025.

Schroeder, J. R.; Crawford, J. H.; Ahn, J.-Y.; Chang, L.; Fried, A.; Walega, J.; Weinheimer, A.; Montzka, D. D.; Hall, S. R.;
845 Ullmann, K.; Wisthaler, A.; Mikoviny, T.; Chen, G.; Blake, D. R.; Blake, N. J.; Hughes, S. C.; Meinardi, S.; Diskin, G.; Digangi, J. P.; Choi, Y.; Pusede, S. E.; Huey, G. L.; Tanner, D. J.; Kim, M.; Wennberg, P. Observation-Based Modeling of Ozone Chemistry in the Seoul Metropolitan Area during the Korea-United States Air Quality Study (KORUS-AQ). Elementa: Science of the Anthropocene 2020, 8, 3. https://doi.org/10.1525/elementa.400.

850 Simpson, D.; Tuovinen, J.-P.; Emberson, L.; Ashmore, M. R. Characteristics of an Ozone Deposition Module. Water, Air, & Soil Pollution: Focus 2001, 1 (5), 253–262. https://doi.org/10.1023/A:1013127826769.

https://doi.org/10.5194/egusphere-2025-6012
Preprint. Discussion started: 5 December 2025

Stevenson, D. S.; Zhao, A.; Naik, V.; O'Connor, F. M.; Tilmes, S.; Zeng, G.; Murray, L. T.; Collins, W. J.; Griffiths, P. T.; Shim, S.; Horowitz, L. W.; Sentman, L. T.; Emmons, L. Trends in Global Tropospheric Hydroxyl Radical and Methane Lifetime since 1850 from AerChemMIP. Atmospheric Chemistry and Physics 2020, 20 (21), 12905–12920. https://doi.org/10.5194/acp-20-12905-2020.

Talukdar, R. K.; Burkholder, J. B.; Schmoltner, A.-M.; Roberts, J. M.; Wilson, R. R.; Ravishankara, A. R. Investigation of the Loss Processes for Peroxyacetyl Nitrate in the Atmosphere: UV Photolysis and Reaction with OH. Journal of Geophysical Research: Atmospheres 1995, 100 (D7), 14163–14173. https://doi.org/10.1029/95JD00545.

Thompson, C. R.; Wofsy, S. C.; Prather, M. J.; Newman, P. A.; Hanisco, T. F.; Ryerson, T. B.; Fahey, D. W.; Apel, E. C.; Brock, C. A.; Brune, W. H.; Froyd, K.; Katich, J. M.; Nicely, J. M.; Peischl, J.; Ray, E.; Veres, P. R.; Wang, S.; Allen, H. M.; Asher, E.; Bian, H.; Blake, D.; Bourgeois, I.; Budney, J.; Bui, T. P.; Butler, A.; Campuzano-Jost, P.; Chang, C.; Chin, M.; Commane, R.; Correa, G.; Crounse, J. D.; Daube, B.; Dibb, J. E.; DiGangi, J. P.; Diskin, G. S.; Dollner, M.; Elkins, J. W.; Fiore, A. M.; Flynn, C. M.; Guo, H.; Hall, S. R.; Hannun, R. A.; Hills, A.; Hintsa, E. J.; Hodzic, A.; Hornbrook, R. S.; Huey, L. G.; Jimenez, J. L.; Keeling, R. F.; Kim, M. J.; Kupc, A.; Lacey, F.; Lait, L. R.; Lamarque, J.-F.; Liu, J.; McKain, K.; Meinardi, S.; Miller, D. O.; Montzka, S. A.; Moore, F. L.; Morgan, E. J.; Murphy, D. M.; Murray, L. T.; Nault, B. A.; Neuman, J. A.; Nguyen, L.; Gonzalez, Y.; Rollins, A.; Rosenlof, K.; Sargent, M.; Schill, G.; Schwarz, J. P.; Clair, J. M. S.; Steenrod, S. D.; Stephens, B. B.; Strahan, S. E.; Strode, S. A.; Sweeney, C.; Thames, A. B.; Ullmann, K.; Wagner, N.; Weber, R.; Weinzierl, B.; Wennberg, P. O.; Williamson, C. J.; Wolfe, G. M.; Zeng, L. The NASA Atmospheric Tomography (ATom) Mission: Imaging the Chemistry of the Global Atmosphere. 2022. https://doi.org/10.1175/BAMS-D-20-0315.1.

Wild, O.; Prather, M. J.; Akimoto, H.; Sundet, J. K.; Isaksen, I. S. A.; Crawford, J. H.; Davis, D. D.; Avery, M. A.; Kondo, Y.; Sachse, G. W.; Sandholm, S. T. Chemical Transport Model Ozone Simulations for Spring 2001 over the Western Pacific: Regional Ozone Production and Its Global Impacts. Journal of Geophysical Research: Atmospheres 2004, 109 (D15). https://doi.org/10.1029/2003JD004041.

Wilson, C. P.; Prather, M. J. Gridded Surface O3, NOx, and CO Abundances for Model Metrics from the South Korean Ground Station Network. Atmospheric Measurement Techniques 2025, 18 (8), 1757–1769. https://doi.org/10.5194/amt-18-1757-2025.

Wilson, C.: Modelling system for computing the tropospheric O3 and CH4 perturbations from South Korean Emissions (KORUS-AQ period), Dryad [code], https://doi.org/10.5061/dryad.f4qrfj78x, 2025.

Wolfe, G. M.; Marvin, M. R.; Roberts, S. J.; Travis, K. R.; Liao, J. The Framework for 0-D Atmospheric Modeling (F0AM) v3.1. Geosci. Model Dev. 2016, 9 (9), 3309–3319. https://doi.org/10.5194/gmd-9-3309-2016.

https://doi.org/10.5194/egusphere-2025-6012
Preprint. Discussion started: 5 December 2025

Woo, J.-H.; Kim, Y.; Kim, H.-K.; Choi, K.-C.; Eum, J.-H.; Lee, J.-B.; Lim, J.-H.; Kim, J.; Seong, M. Development of the CREATE Inventory in Support of Integrated Climate and Air Quality Modeling for Asia. Sustainability 2020, 12 (19), 7930. https://doi.org/10.3390/su12197930.

Yan, C.; Tham, Y. J.; Zha, Q.; Wang, X.; Xue, L.; Dai, J.; Wang, Z.; Wang, T. Fast Heterogeneous Loss of N2O5 Leads to Significant Nighttime NOx Removal and Nitrate Aerosol Formation at a Coastal Background Environment of Southern China. Science of The Total Environment 2019, 677, 637–647. https://doi.org/10.1016/j.scitotenv.2019.04.389.

Zhang, L.; Brook, J. R.; Vet, R. On Ozone Dry Deposition—with Emphasis on Non-Stomatal Uptake and Wet Canopies. Atmospheric Environment 2002, 36 (30), 4787–4799. https://doi.org/10.1016/S1352-2310(02)00567-8.

Zhang, L.; Vet, R.; O'Brien, J. M.; Mihele, C.; Liang, Z.; Wiebe, A. Dry Deposition of Individual Nitrogen Species at Eight Canadian Rural Sites. Journal of Geophysical Research: Atmospheres 2009, 114 (D2). https://doi.org/10.1029/2008JD010640.

Ziemke, J. R.; Oman, L. D.; Strode, S. A.; Douglass, A. R.; Olsen, M. A.; McPeters, R. D.; Bhartia, P. K.; Froidevaux, L.; Labow, G. J.; Witte, J. C.; Thompson, A. M.; Haffner, D. P.; Kramarova, N. A.; Frith, S. M.; Huang, L.-K.; Jaross, G. R.; Seftor, C. J.; Deland, M. T.; Taylor, S. L. Trends in Global Tropospheric Ozone Inferred from a Composite Record of TOMS/OMI/MLS/OMPS Satellite Measurements and the MERRA-2 GMI Simulation. Atmospheric Chemistry and Physics 2019, 19 (5), 3257–3269. https://doi.org/10.5194/acp-19-3257-2019.

Zhao, Y.; Zheng, B.; Saunois, M.; Ciais, P.; Hegglin, M. I.; Lu, S.; Li, Y.; Bousquet, P. Air Pollution Modulates Trends and Variability of the Global Methane Budget. Nature 2025, 642 (8067), 369–375. https://doi.org/10.1038/s41586-025-09004-z.